Immunologic Research (2025) 73:27
https://doi.org/10.1007/s12026-024-09557-7

RESEARCH

Inactivation of ATG13 stimulates chronic demyelinating pathologies in muscle-serving nerves and spinal cord

Molly E. Drosen[1,2] · Sarojini Bulbule[2] · Gunnar Gottschalk[2,3] · Daniel Peterson[4] · Linda Adrienne Allen[1] · Leggy A. Arnold[1] · Avik Roy[1,2,3]

Received: 9 April 2024 / Accepted: 18 November 2024

Abstract

Chronic muscle fatigue is a condition characterized by debilitating muscle weakness and pain. Based on our recent finding to study the potential effect of mTOR on ATG13 inactivation in chronic muscle fatigue, we report that biweekly oral administration with MHY1485, a potent inducer of mTOR, develops chronic illness in mice resulting in severe muscle weakness. As a mechanism, we observed that MHY1485 feeding impaired ATG13-dependent autophagy, caused the infiltration of inflammatory M1 macrophages (Mφ), upregulated IL6 and RANTES by STAT3 activation, and augmented demyelination in muscle-serving nerve fibers. Interestingly, these mice displayed worsened muscle fatigue during 2-day post-treadmill exercise, suggesting the critical role of chronic mTOR activation in potential PEM pathogenesis. Interestingly, ATG13-repressor mice exhibited enhanced infiltration of M1Mφ cells, STAT3 activation, demyelination of nerve fibers, and PEM-like symptoms, suggesting the potential role of ATG13 impairment in post-exertional fatigue.

Highlights

- The potential role of mTOR activation in post-exertional fatigue is highlighted.
- As a molecular mechanism, mTOR activation augments autophagy impairment via ATG13 inactivation.
- Autophagy impairment induces IL-6 and RANTES via STAT3, demyelinates nerves in the muscle and spinal cord.
- ATG13 repressor mice (Tg-ATG13) displayed inflammatory demyelination and post-treadmill fatigue.

✉ Avik Roy
aroy@simmaron.com

[1] Milwaukee Institute for Drug Discovery, Department of Chemistry & Biochemistry, University of Wisconsin-Milwaukee, 2000 E Kenwood Blvd, Milwaukee, WI 53211, USA

[2] Simmaron R&D Lab, 2000 E Kenwood Blvd, Suite # 320, Milwaukee, WI 53211, USA

[3] Simmaron Research Institute, 948 Incline Way, Incline Village, NV 89451, USA

[4] Sierra Internal Medicine, Incline Village, NV 89451, USA

Published online: 07 January 2025

Graphical abstract

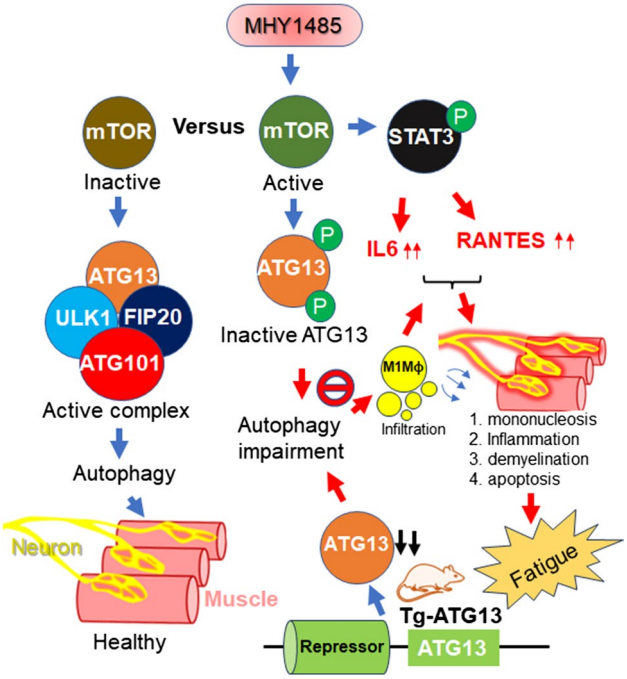

Keywords Chronic demyelinating pathologies · MTOR-ATG13 crosstalk · ME/CFS

Abbreviations

mTOR	Mammalian target of rapamycin
mTORC1	MTOR complex 1
EMG	Electromyogram
PEM	Post-exertional malaise
ATG13	Autophagy-related protein 13
ULK1	Unc-51 like autophagy activating kinase1
LC3	Microtubule-associated protein 1A/1B-light chain 3
STAT3	Signal transducer and activator of transcription 3
RANTES	Regulated upon Activation, Normal T cell Expressed, and Secreted
IL-6	Interleukin 6
IP	Immunoprecipitation
IB	Immunoblot
ChIP	Chromatin immunoprecipitation
MFI	Mean fluorescence intensity
Bwt	Body weight
Mφ	Macrophage
DAB	Diaminobenzidine
IF	Immunofluorescence
ir	Immunoreactive

Introduction

ME/CFS is a chronic inflammatory disease characterized by severe muscle fatigue, pain, and cognitive impairment [1]. The most reliable pathological symptom of ME/CFS is post-exertional malaise (PEM) [2], which is persistent muscle fatigue and pain after treadmill exercise [3, 4]. Upon treadmill exercise, patients are often reported to have a "crash" or "collapse" with severe and prolonged mental and physical tiredness [5, 6]. Sometimes, the post-exertional fatigue becomes so severe that the patient remains bedridden for a long time [6]. However, until now, the molecular mechanism of PEM is poorly understood, primarily due to the unavailability of a reliable disease model that successfully displays PEM pathology after treadmill exercise.

Recently, our research [7] identified that ATG13, an early autophagy protein, was phosphorylated and elevated in the serum of a small cohort ($n = 10$) of ME/CFS patients, suggesting a potential role of ATG13 inactivation and subsequent autophagy impairment in ME/CFS. ATG13 initiates autophagosome formation by forming a core complex with ULK1 (Unc-51 Like Autophagy Activating Kinase 1), FIP200, and ATG101 [8]. The mammalian target of rapamycin complex 1 (mTORC1), an intracellular serine/threonine kinase complex, phosphorylates

ATG13 at its serine residue, disrupts the formation of an autophagy complex, and as a result, the autophagy process is inhibited [9, 10]. Interestingly, our research [7] also identified that the serum samples of ME/CFS patients were associated with elevated levels of phosphorylated ATG13 in serine residue. That phosphorylated ATG13 was observed to induce microglial activation via engagement with the receptor of advanced glycoprotein, or RAGE. Since the phosphorylation of ATG13 was augmented due to the upstream activation of mTORC1 [11], we are interested in studying the crosstalk between mTOR and ATG13 in the pathogenesis of ME/CFS. Therefore, in our current paper, we attempted to make a drug-induced mouse model with a chemical induction of mTORC1 by the compound MHY-1485. MHY-1485 is a potent cell-permeable mTOR activator [12, 13] that targets the ATP domain of mTOR. A cell culture study demonstrated that MHY1485 inhibited the autophagy process in HEK293T cells by inhibiting the fusion of the autophagosome with the lysosome [12]. Moreover, a cell culture study suggests that MHY-1485 potentially promotes fertility in females once treated in combination with an AKT agonist [14]. However, the effects of MHY1485 in the chronic activation of mTOR, autophagy impairment, inflammatory changes, and resultant muscle fatigue had not been tested in vivo.

A dose-dependent feeding study followed by a bilateral EMG recording analysis demonstrated that oral administration of 5 mg/kg bwt MHY-1485, a selective agonist of mTOR, once an alternative day for 2 weeks induced S355 phosphorylation of ATG13, autophagy impairment, and severe muscle fatigue in 3- to 4-week-old female B6 mice. Immunohistochemical studies in muscle biopsies revealed that the mTOR-mediated autophagy impairment induced an elevated infiltration of M1 macrophages (M1Mϕ), demyelinating response in nerve bundles and nerve fibers serving skeletal muscle, and apoptosis in muscle cells. While investigating the molecular mechanism, our research highlighted that the chronic activation of mTOR triggered the activation of STAT3 following upregulations of inflammatory cytokines such as IL6 and RANTES. The direct role of ATG13 inactivation in muscle fatigue was further corroborated by a post-treadmill fatigue assessment study in our in-house transgenic ATG13 suppressor mouse model (Tg-ATG13), in which a single-session treadmill exercise at a speed of 14 rpm for 7 min exacerbated muscle fatigue even after 2 days. Taken together, our present study highlighted a molecular mechanism of chronic mTOR activation in ATG13 inactivation to trigger a demyelinating response resulting in chronic muscle fatigue in mice.

Materials and methods

Reagents, plasmids, and antibodies

MHY1485 (Cat # B5853), puromycin (Cat #A3740; 50 mg), and Ampicillin (Cat #A2510; 1 g) were purchased from Apex Bio (Houston, TX). Luria Broth (Miller's) powder (100 g) was purchased from Innovating Science. Methylcellulose solution (3%) (CAS No.: 9004–67-5) was purchased from Carolina (Burlington, NC). HA-hULK1 was a gift from Do-Hyung Kim (Addgene plasmid # 31,963; http://n2t.net/addgene:31963; RRID: Addgene_31963). FLAG-hAtg13 plasmid was a gift from Noboru Mizushima (Addgene plasmid # 22,872; http://n2t.net/addgene:22872; RRID: Addgene_22872). GFP-LC3 plasmid was a gift from Jayanta Debnath (Addgene plasmid # 22,405; http://n2t.net/addgene:22405; RRID: Addgene_22405). Cloning of IL6 promoter and site-directed mutation of IL6 promoter were performed by GeneCopoeia (Rockville, MD). HEK293T cells and C20 human microglial cell line were gifted by Prof. Leggy A. Arnold of the University of Wisconsin-Milwaukee. All antibodies were enlisted below in Table 1 detailing dilution, application, and vendors.

RayBio® C-Series Human Inflammation Antibody Array (Cat# AAH-INF-3) was purchased from RayBiotech (Norcross, GA 30092). A Human IL6 ELISA kit was purchased from BD Biosciences (Cat#555220). The Human RANTES ELISA kit was purchased from Abcam (Cat# ab100633). SuperScript® III Platinum® SYBR® Green One-Step qRT-PCR Kit, 100 rxns (Cat # 11736051; Lot#2,416,961) was purchased from Life Technologies (ThermoFisher Scientific). IRDye® 700 STAT3 Consensus Oligonucleotide for EMSA was purchased from LI-COR Bioscience (P/N: 829–07922). Novex™ WedgeWell™ 4–12% Tris–Glycine gel (Cat# XP04122BOX; Lot # 21,122,230) for immunoblot and 6% DNA retardation gel (Cat# EC6365BOX; Lot# 22,012,742) for EMSA were purchased from Invitrogen (ThermoFisher Scientific). LysoTracker™ Red DND-99 (Cat # L7528) was purchased from ThermoFisher Scientific.

Animal housing and treatment

Male and female B6 mice (3- to 4-week and 5- to 6-week old) were purchased from the Jackson Laboratory. The animal maintenance, behavioral analysis, and surgical procedure were approved by the IACUC (protocol: 21–22#28) and IBC (protocol#B22.014) committees of the University of Wisconsin-Milwaukee (UWM). Mice were housed in ventilated micro-isolator cages in an environmentally controlled vivarium (7:00 A.M./7:00 P.M. light cycle; temperature maintained at 21–23 °C; humidity 35–55%) at the animal research center (ARC) of UWM. Tg-ATG13 mouse strain [MO-146703355 (041527-UCD-RESUS)] was developed by the Mutant Mouse Resource and Research Center (MMRRC) of UC Davis upon request. These animals were maintained, genotyped, bred, and tested under

Table 1 List of antibodies and applications

Antibody	Host/isotype	Vendor (catalogue)	Application	Dilution
Anti-HA	Rabbit / IgG	Proteintech (51,064–2-AP)	WB	1:500
Anti-FLAG	Mouse / IgG2b	Proteintech (66,008–4-1 g)	WB	1:500
Anti-LC3	Rabbit / IgG	Proteintech (14,600-I-AP)	WB	1:500
Anti-IL6	Rabbit / IgG	Proteintech (21,865–1-AP)	WB	1:500
Anti-βactin	Mouse/IgG	RnD Systems (MAB8929)	WB	1:1000
Anti-Phospho (Y705) STAT3	Rabbit / IgG	Cell Signaling Tech (9145 T)	WB/IHC/IF	1:500
Anti-Phospho (S727) STAT3	Rabbit / IgG	Cell Signaling Tech (9134 T)	WB	1:500
Anti-ATG13	Rabbit/IgG	Invitrogen (18258-1-AP)	WB	1:500
Anti-Phospho (S355) ATG13	Rabbit/IgG	Cell Signaling Tech (46329S)	WB	1:500
Anti-Tuj1	Mouse/IgG	Invitrogen (MA1-118)	IF	1:500
Anti-WDFY3	Mouse/IgG	Invitrogen (MA5-48,715)	IF/IHC	1:500
Anti-IBA1	Rabbit/IgG	Millipore Sigma (ZRB1177)	IF	1:500

WB western blot, *IF* immunofluorescence, *IHC* immunohistochemistry

protocol no. 22–23 #20. Animals were provided standard mouse chow and water ad libitum and closely monitored for health and overall well-being daily by veterinary staff and the investigator. After 2 days of resting period, mice were gavaged with 0, 2, 5, and 10 mg/kg bwt MHY1485 with a micro-cannulated blunt-tipped gavage needle (24G curved) every alternate day for 2 weeks. MHY1485 was suspended in 0.05% (v/v) methylcellulose solution. Before feeding, animals were weighed, and vitals such as body temperature and heart rate were monitored with MouseStat Jr. (Kent Scientific). In the beginning, a pilot study ($n = 5$) was performed for dose optimization, tolerance, age, and gender sensitivity of the drug. Later, the same study was repeated with $n = 10$ animals per group. After 2 weeks of feeding, animals were monitored for gross movement, EMG recording, and post-treadmill analysis for another 7 days. After that, molecular studies were performed in muscle, brain, and splenic tissue. Results are confirmed with three different experiments at $p < 0.05$ significance.

Collection of human serum samples

Serum samples were collected, and the questionnaire data were previously collected [7] under the supervision of Dr. Daniel Peterson (Sierra Internal Medicine, Incline Village, NV) (Western IRB#20,201,812). Blood samples were centrifuged, and serum samples were aliquoted and then immediately frozen at − 80 °C. Each sample was given a unique identification number and recorded both in a notebook and Microsoft Excel with a date and signature as per the IRB-approved protocol. Samples were then delivered to our research facility in UWM on dry ice overnight. Upon receipt, samples were processed and assayed immediately. Questionnaire and de-identified clinical data are stored in a secure, limited-access Redcap sever database managed by the Research Staff and Clinical Fellow at Sierra Internal Medicine. Patient records were maintained with privacy policy guidelines set by Sierra Internal Medicine. The sample cohort used in the study was previously reported elsewhere [15].

Promoter analysis and chromatin immunoprecipitation (ChIP) assay

Promoter sequences of IL6 and RANTES were extracted from chromosomes #7 (PubMed.gov Seq. ID: NG_011640.1) and 17 (PubMed.gov Seq ID: 259,906,039), respectively. After that, with the help of MatInspector (Genomatix software suite), these sequences were analyzed for STAT3 binding sites; resultant responsive elements of STAT3 protein were identified with matrix match score > 0.9 and then displayed with a bit score diagram. Next, primer sequences were designed from 125 to 150 bp of nucleotides around the response element. Primer designing was performed with the help of the "primer blast" module of PubMed (Link: https://www.ncbi.nlm.nih.gov/tools/primer-blast/). Primers used to amplify sonicated DNA are as follows.

IL6 promoter (product length = 145 bp)

Sense: 5′AGACCTGGTTTGGGGATCTTAAT 3′; Antisense: 5′AGCAATGAGCTGGTCTCCCA 3′.

RANTES promoter (product length = 90 bp)

Sense: 5′ TGTTGTCCCCAAGAAAGCGG 3′; Antisense: 5′ GGAAAAATTTCTCTGCTGACATCCT 3′.

Recruitment of STAT3 to the IL6 and RANTES promoters had been analyzed in mouse primary microglial cells

in vitro by ChIP as described previously [16]. Briefly, cells were treated with 5 µM MHY1485 for 5 h under serum-free condition, fixed with 4% paraformaldehyde, quenched with 5 M glycine, washed, extracted for nuclear fraction (Abcam nuclear extraction kit; Cat# ab113474), sonicated (Swift lab ultrasonic processor; pulse sonication at 25 kHz) in Tris–EDTA buffer (Ph 7.6), incubated with antibodies at rotating condition overnight followed by pulling down with protein A agarose, dissociated the DNA–protein complex with Chelex® 100 (Sigma), centrifuged, and then performed real-time PCR with aforementioned primers via SYBR Green detection method.

Electrophoretic mobility shift assay (EMSA)

EMSA was performed in mouse microglial cells as described below. Mouse primary microglial cells were treated with 0, 2, and 5 µM MHY1485 for 2 h, followed by nuclear fractionation with a nuclear extraction kit (Abcam). After that, the reaction was performed with 2 µL 10X Binding Buffer (100 mM Tris, 500 mM KCl, 10 mM DTT; pH 7.5) + 1 µL of Poly(dI•dC) 1 µg/µL in 10 mM Tris, 1 mM EDTA; pH 7.5 + 2 µL of 25 mM DTT/2.5% Tween®20 + 10 µL of water + 1 µL of IRDye 700 NFκB + 2 µL of nuclear extract (5 µg) (= total 20 µL reaction). During that reaction, 6% DNA gel was pre-run at 0.5% TBE for 30 min (120 V), and then the reaction mixture was loaded and electrophoresed for 90 min at 90 V. The gel was carefully transferred in a glass tray and imaged at Li-Cor Odyssey Sa imager at 200 µm resolution.

GFP-LC3 and Lysotracker fluorimetry assay

HEK293T cells were cultured in a 96-well plate for fluorimetry and in an 8-well chamber slide for immunofluorescence imaging. Once reached 75% confluency, cells were transfected with 0.25 µg of GFP-LC3 plasmid via Lipofectamine™ 3000 transfection reagent as per the manufacturer's protocol. After 24 h, cells were starved for an additional 24 h to induce autophagy and then treated with increasing doses of MHY1485 for 5 h. Dose-dependent effect of MHY1485 on the expression of GFP-LC3 was assessed by fluorimetric reading at Ex: Em = 485/535 nm in the Victor × 3 fluorescence platereader. For lysosomal quantification, cells were labeled with 50 nM of LysoTracker™ Red DND-99 (initial conc: 1 mM; diluted with serum-free media 1:20,000) and incubated at 37 °C for 30 min. For fluorimetry, cells were scanned at Ex: Em = 540/576 nm in a Victor × 3 fluorescence plate reader. For immunofluorescence, cells were fixed with chilled methanol, kept at − 20 °C overnight, washed with 1 X PBS, and then imaged at a Hund Wetzlar fluorescence microscope at the FITC (GFP-LC3) and TRITC (Lysotracker) channels.

Real-time PCR analysis

RNA isolation was performed with a Gene Jet RNA purification kit (Lot # 01199835; Thermo Scientific) provided with RNA purification columns, lysis buffer, wash buffers (1 & 2), and elution buffer. Briefly, 300 µL of lysis buffer (supplemented with βME) was added in each well of 6 wells with 75% confluent microglial cells, or in another case, 25 µg of homogenized muscle tissue was lysed with 500 µL of lysis buffer, passed through the purification column, washed with wash buffers, and then eluted with elution buffer. After RNA isolation, 1 µg of RNA was analyzed for PCR via a SYBR green detection strategy with the help of SuperScript® III Platinum® SYBR® Green One-Step qRT-PCR Kit. Relevant primers of IL6 and RANTES were designed by the "Pick primer" module of the https://ncbi.nlm.nih.gov/ online tool.

Immunoblot assay

Immunoblot assay was performed as described before [7]. Briefly, cells and tissue lysates were mixed with 5X Laemmli buffer, electrophoresed in 4–12% Tris–Glycine gel in tris–glycine SDS running buffer, transferred in a nitrocellulose membrane (P/N 926–31,090; Li-Cor Biosciences, Lincoln, NE) in tris–glycine transfer buffer, incubated with appropriate primary antibodies overnight under shaking condition, labeled with IRDye700 and 800-tagged secondary antibodies for 2 h at r.t in an orbital shaker, and then imaged in Odyssey Sa imager at 200 µm resolution.

Immunohistochemical analyses

Immunohistochemical (IHC) analyses were performed as described elsewhere [17]. Briefly, muscle and brain tissue were mounted in a paraffin-embedded block and then sectioned at a thickness of four microns (Children's Research Center, Medical College of Wisconsin, Milwaukee, WI). Paraffin-embedded sections were then processed through a series of dippings in Coplin jar chambers filled with Xylene, 100%, 70%, 50%, and 20% ethanol, and finally rehydrated with water as per standard IHC protocol. After that, blocking was performed with 2% BSA-containing blocking buffer and then treated with primary antibodies overnight in a humidified chamber at room temperature. Next, tissue sections were washed three times with 1X PBST (PBS + 0.05% Tween) buffer, followed by incubation with a biotinylated secondary antibody. For double labeling, AP (alkaline peroxidase)-tagged anti-rabbit and biotin-tagged anti-mouse antibodies were used as recommended by the dual IHC kit (Abcam dual IHC Kit; Cat # ab210059). For immunofluorescence (IF) analysis, FITC- and TRITC- conjugated mouse and rabbit

2° antibodies (Jackson ImmunoResearch) were used. Briefly, tissue slides were deparaffinized, retrieved for antigen by the citrate buffer (pH 5.5), blocked with 2% horse serum, treated with primary antibodies (1:100–1:250 dilution), washed with 1 X TBST (3 times), incubated with FITC- or TRITC-labeled antibodies, washed again with 1XTBST (3 times; added DAPI in the final wash), and finally cover slipped. Images were captured by an Olympus fluorescence microscope.

MFI (mean fluorescence intensity) was counted by Fiji-ImageJ software. Briefly, the image of interest was opened from the "File" tab, followed by splitting channels from the "Color" option of the "Image" tab. Then, the green or red channel images were selected for MFI calculation by selecting the "Mean gray value" under the "Set Measurements" of the "Analyze" tab. After that, the polygon tool was used to select the region of interest, and the MFI value was acquired by clicking the "Ctrl + M" button on the keyboard.

Cell counting was performed in CaptaVision + software (Accu-Scope Inc.). Briefly, the image was opened and calibrated to 6 pixel/μm unit based on the resolution of the raw image. Under the "Measure" tool, the "Manual Class counting" option was selected, followed by clicking on each target cell.

We performed Bielschowsky's silver staining to determine myelin integrity as described elsewhere [18]. Briefly, the slide was deparaffinized, stained with 10% silver nitrate, washed with dH2O, incubated with silver hydroxide, followed by washing with 0.1% ammonium hydroxide, and finally developed color with a developing solution of 0.2 ml 37% formaldehyde, 12 ml dH2O, 12.5 μL 20% nitric acid, 0.05 g citric acid, and 50 mL silver hydroxide.

Behavioral assessment of muscle fatigue: grip strength, EMG, treadmill exercise, and gross movement analysis

Muscle fatigue was assessed by grip strength analysis. The grip strength apparatus is a metal T-shaped hook, which is attached to a wooden horizontal bar tightly fixed with a wooden pole. The hook is placed 10 in. high from the cage top so that the mouse can safely land on the cage if it fails to grip the hook or is unable to suspend freely. Grip strength latency is the time taken to remain on the bar before landing on the cage top. Untreated control mice grip the bar, curl up the body, and then climb on the apparatus freely. The test is terminated after 180 s if the mouse does not come down willingly to the cage. The affected mouse was found to be incapable of holding the bar, suspending the body, or even climbing up on the hook. The latency was recorded by a stopwatch.

For EMG recording, the mouse was anesthetized and placed on a surgical table with the dorsal side facing up. The fur layer was carefully cut so that the biceps femoris muscles were exposed in both hind limbs. The lumbar region of the spinal cord was also made visible. Surface electrodes were placed on both sides of the femoral muscle, and the reference electrode was placed on the lumbar spinal cord. The fur was carefully placed in its original position, sealed with surgical glue, and allowed the animal to completely awaken. The three-pronged surface electrodes were placed on the muscle surface and attached with self-adhesive fabric. The fur layer was carefully stitched with tissue adhesive. Saline (0.9% NaCl) was injected intraperitoneally immediately after surgery, and the subsequent recovery was performed in a heated pad. Once fully regained consciousness, EMG recording was performed both in control and diseased mice ($n = 5$). The EMG signals were recorded in ADInstruments Powerlab and then amplified (Bio Amp Powerlab) at a sampling rate of 2 kHz. The result was displayed in Chart software at a resolution of 10–50 μV. The reference was recorded at a range of − 5 to 5 mV.

Columbus XR4 (S/n APM933AT-I) mouse treadmill was used to evaluate muscle fatigue in mice. Briefly, each mouse was placed on a motorized conveyor belt. Initial preconditioning was conducted at low speed (5 rpm) for 1 min, and then the speed increased to 15 rpm for another 14 min. The end of the track was blocked with cardboard to prevent escape.

After the treadmill exercise, each mouse was evaluated for gross movement in an open-field acrylic arena (Stoelting Co; Cat # 60,100). The arena is a 40-cm square box with a transparent wall and detachable fiber base designed for easy cleaning. The movement was recorded with the Stoelting digital USB camera (Cat#10–000–332) attached to the ceiling from a suspension bar. The camera is linked to ANY-maze video tracking software with the connecting cable. For each trial, horizontal activity, total distance, movement time, resting time, and tracking plot were derived. Each recording was performed after 2 min of the acclimatization period.

Barnes maze

Barnes maze analysis was performed as described elsewhere [19]. The Barnes maze was a blue metal circular apparatus which is 75 cm in diameter (Stoelting™ 60,270) and placed on a tripod stand. This maze contains 19 false square boxes at a 5 cm gap and one escape box, which was attached to a black escape tunnel underneath. Distinct spatial cues were located all around the maze and were kept constant throughout the study. To explore if the treadmill exercise impaired the hippocampus-dependent spatial learning abilities in mice, we performed Barnes maze analysis in these mice once the Treadmill study was completed (day 5 after treadmill exercise). Each mouse was trained 3 times a day for 2 consecutive days. Day 3 is a resting day, and day 4 is

a test day. During the test, each mouse was carefully placed in the middle of the arena inside of a cylindrical start chamber. After 10 s, the start chamber was removed, and the mouse was allowed to move around the maze to find the escape tunnel. The session ended when the mouse entered the baited tunnel. Total time (latency), errors (no. of false attempts before finding the escape tunnel), and track plot were acquired by the ANY-Maze video tracking software.

Statistical analysis

Results were confirmed by three different experiments in $n = 10$ animals per group. Following is the justification of animal numbers. $N = \frac{z^2 \times p(1-p)}{\varepsilon^2} = \frac{1.28^2 \times 0.99(1-0.99)}{0.05^2} = 7$. For adverse outcomes, three additional animals were included per group. Therefore, $N = 10$ animals per group. $N =$ sample size; Z is the z score, which is 1.28 for power 0.8; p is the population proportion. For a 99% confidence interval, p will be 0.01. (1–p) = (1–0.01) = 0.99; ε is the margin of error = 0.05. There was no bias in gender selection in the initial stage of the project. However, MHY1485 feeding caused fatigue only in female mice. For two groups, either an unpaired t-test or non-parametric Mann–Whitney U test (due to low sample size and failure to pass the normality test) was adopted with $p < 0.05$. For more than one group, a one-way ANOVA was adopted considering treatment of MHY1485 or genotype as a single effector. ROUT outlier handing analysis was performed before running one-way ANOVA. Tukey's posthoc analysis was performed to test the homogeneity of variances.

Results

MHY1485 induces chronic muscle fatigue in 3- to 4-week-old female B6 mice

In ME/CFS patients, ATG13 was found to be inactivated by serine phosphorylation and upregulated in the serum [7]. Since the ATG13 is a downstream target of mTOR, next, we wanted to study the role of chronic activation of mTOR in the pathogenesis of chronic muscle fatigue. To test the role of chronic activation of mTOR, we first adopted a molecular strategy to chemically induce mTOR activation in mice. In our current study, MHY1485, a selective agonist of mTOR, was suspended at 0.5% methylcellulose and orally gavaged at a dose of 2, 5, and 10 mg/kg bwt ($n = 10$ per group) to 3- to 4-week-old B6 mice every alternate day for 14 days (Schema: Supplementary Fig. 1A). Before feeding, mice were randomized based on gender and divided into four groups: vehicle, 2, 5, and 10 mg/kg bwt MHY1485. Health vitals such as initial body weight, body temperature, and blood pressure were recorded. After 1 week, significant mortality was noticed in the 10 mg/kg bwt group as 50% of female mice were deceased (Supplementary Fig. 1B). However, there was no mortality observed in female mice with 2 and 5 mg/kg bwt groups. These mice survived acute vital changes such as hypothermia (Supplementary Fig. 1C), reduced blood pressure (Supplementary Fig. 1D), and frequent freezing episodes until 7 days after the first dose. After that, these mice regained normal body temperature and blood pressure, even though the heart rate was observed to be lower until 2 weeks of feeding. Both 2 and 5 mg/kg groups survived until the end of the experiment timeline (1 month after the last dose) with severe fatigue. Interestingly, feeding with 5 mg/kg bwt MHY1485 resulted in significant immobility in 70% of female mice ($n = 7$ out of 10).

Apparently, female mice in 5 mg/kg bwt MHY1485 displayed slow movement with periodic freezing at resting conditions. These mice did not gain any body weight (Supplementary Fig. 1E) and size (Fig. 1A) when compared with vehicle-fed mice throughout the study, suggesting that MHY1485 might cause a significant deficit in muscle growth. While studying the drug metabolism, our pharmacokinetic (PK) study revealed that the serum level of MHY1485 increased as early as 15 min, achieved maximum at 45 min, and retained until 6 h after a single gavaging of MHY1485 at a dose of 5 mg/kg bwt (Fig. 1B).

Interestingly, male mice across all different groups gained body weight and size over time. That observation intrigued us to study muscle fatigue in these female mice. Muscle fatigue can be quantitatively monitored with the EMG recording method. Therefore, next, we performed EMG recording under resting conditions (Fig. 1C). Briefly, two 2 mm electrodes were placed bilaterally on the surface of the left and right biceps femoris muscle, and a reference electrode was placed at the center position on the lower spinal cord (Fig. 1C). The EMG recording was performed at a resolution of 50 µV and the reference recording at 3 mV resolution. Vehicle-fed mice displayed characteristic normal EMG waves (Fig. 1D (i and ii)), whereas mice treated with 5 mg/kg bwt MHY1485 displayed an abnormal pattern of EMG waves with repetitive bursts followed by inactivity indicating potential myokymic changes (Fig. 1D (iii and iv)) in the muscle. Myokymic waves are characteristic of inflammatory denervation at muscle fibers. The reference electrode was placed in the spinal cord, and EMG signals through the reference electrode displayed a consistent pattern of waves in both groups (Fig. 1E). To further confirm muscle fatigue, we performed grip strength analyses on these mice (Fig. 1F; (i and ii)). Accordingly, increasing doses of MHY1485 were found to reduce grip strength latency in female mice (Fig. 1F (iii)) with a significant drop after 4 days of feeding and continued to be decreased with increasing time of feeding. Moreover, gross movement analyses in the ANY-maze open-filed arena (Stoelting Company, IL) (Fig. 1G, H) followed

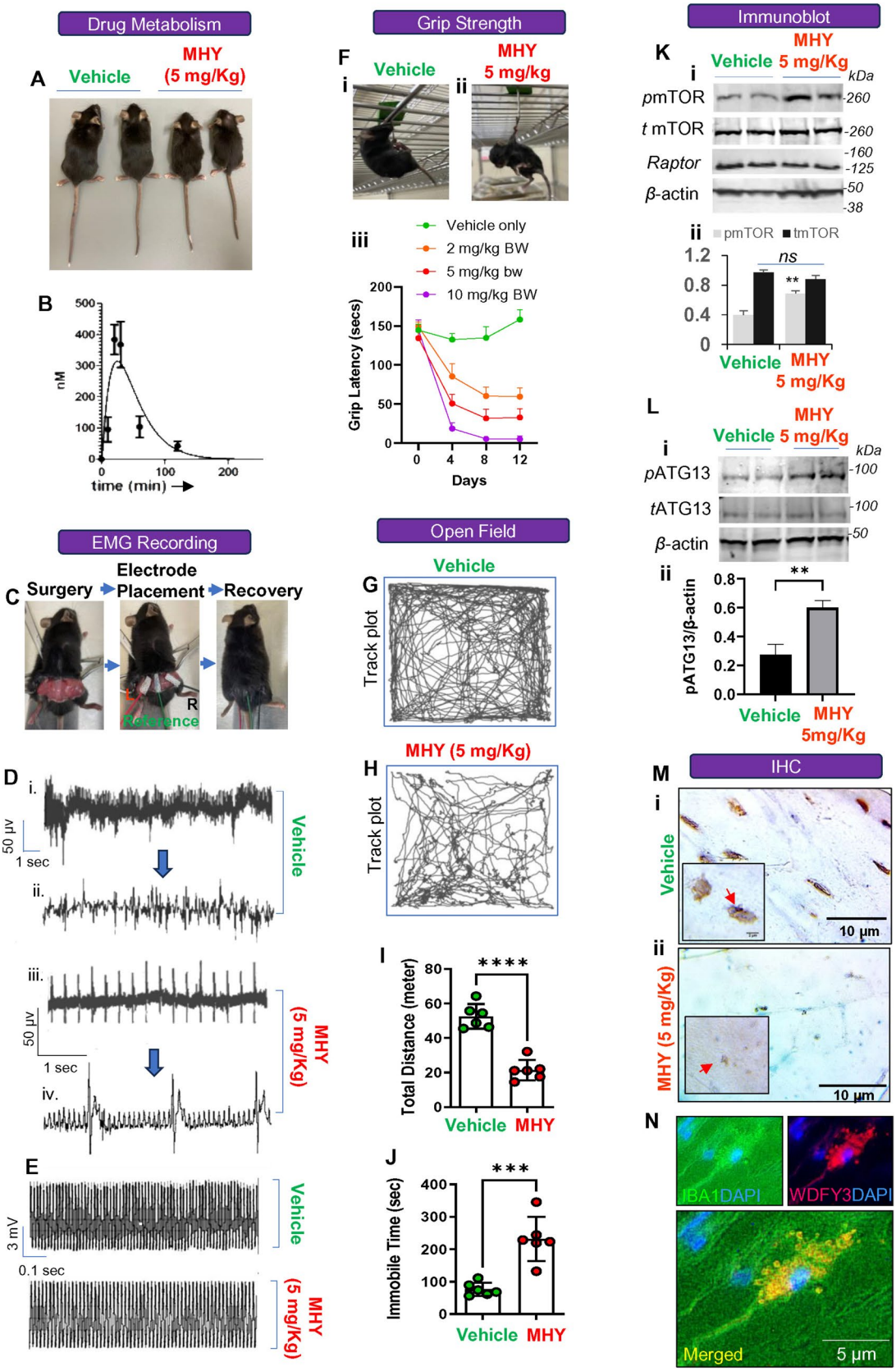
Drug Metabolism
A
Vehicle
MHY (5 mg/Kg)
B
nM
time (min)
Grip Strength
F
i
Vehicle
ii
MHY 5 mg/kg
iii
Vehicle only
2 mg/kg BW
5 mg/kg bw
10 mg/kg BW
Grip Latency (secs)
Days
Immunoblot
K
i
Vehicle
MHY 5 mg/Kg
kDa
pmTOR
t mTOR
Raptor
β-actin
ii
pmTOR
tmTOR
ns
L
pATG13
tATG13
pATG13/β-actin
EMG Recording
C
Surgery
Electrode Placement
Recovery
Reference
D
50 µv
1 sec
Vehicle
MHY (5 mg/Kg)
E
3 mV
0.1 sec
Open Field
G
Vehicle
Track plot
H
MHY (5 mg/Kg)
I
Total Distance (meter)
J
Immobile Time (sec)
IHC
M
10 µm
N
IBA1DAPI
WDFY3DAPI
Merged
5 µm

◂**Fig. 1** MHY1485 induces muscle fatigue in female B6 mice. **A** Three- to four-week-old B6 mice ($n=10$; 5 male + 5 female/group) were orally administered with MHY1485 (labeled as "MHY"; mixed with 0.05% methylcellulose), every alternate day for 2 weeks. Representative images displayed the difference in body lengths between vehicle and 5 mg/kg MHY-fed animals. **B** Pharmacokinetic (PK) study to assess the bioavailability of MHY1485 in serum samples of mice ($n=3$) after 0, 15, 30, 60, 90, 120, and 180 min of feeding via gavage. Results are mean ± SEM of three independent experiments. **C** Electrode placement strategy followed by **D** spontaneous EMG recording on the biceps femoris muscle of B6 mice. L stands for left, R for right, and the middle electrode is the reference electrode. The low-resolution unmagnified and high-resolution magnified EMG waves were shown for vehicles (i and ii) and (iii and *iv*) MHY1485-fed mice, respectively. **E** Reference EMG waves were observed to be consistent between groups. **F** Grip strength analysis in (i) the vehicle and (ii) MHY groups displayed significantly reduced (iii) latency measured on 4-, 8-, and 12-days post-drug treatment. $^{**}p<0.001$ and $^{***}p<0.0005$ versus respective vehicle groups. The significance of the mean was tested with two-way ANOVA considering *treatment* and *days* as two effectors. Track plots represented gross motor activities of **G** vehicle- and **H** MHY-fed animals in open-field apparatus. **I** Total distance and **J** immobile time were measured in the vehicle (green dots) and MHY-fed (red dots) groups ($n=8$ per group). $^{****}p<0.0005$ and $^{***}p<0.001$ versus MHY group compared to vehicle-fed group as derived by Mann–Whitney non-parametric test. Results are mean ± SEM of three independent experiments. **K** (i) Immunoblot assay of S2448phospho-mTOR (*p*mTOR), total mTOR (*t* mTOR), Raptor, and beta-actin (β-actin) were performed in muscle lysate. (ii) Relative densitometry analyses of *t*mTOR and *p*mTOR after normalizing with respective β-actin band densities (ImageJ software). $^{**}p<0.01$ versus control as derived by an unpaired *t*-test. **L** (i) Immunoblot analyses of S355phospho-ATG13 (*p*ATG13)), total ATG13 (*t*ATG13), and beta-actin were performed in the biceps muscle. (ii) Relative densitometry analysis indicated $^{**}p<0.01$ (=0.0028) versus vehicle. **M** Representative images are WDFY3-stained muscle tissue sections of (i) vehicle and (ii) MHY1485 (5 mg/kg)-fed mice ($n=5$). Insets are high-magnification images. Arrowheads indicate autophagosomes. **N** Dual immunofluorescence analysis of IBA1 (green) and WDFY3 (red) to detect the autophagosomes (WDFY3-*ir* red circles) in macrophage cells infiltrated in muscle tissue of vehicle-fed mouse. The detailed quantification analyses were performed in Supplementary Fig. 5. All raw blots were shown in Supplementary Fig. 10 and dotted histogram analysis for the quantification of autophagosome counts was shown in Supplementary Fig. 4

by the assessment of the total distance traveled (Fig. 1I) and immobility time (Fig. 1J) confirmed that mice fed with 5 mg/kg bwt MHY1485 displayed significant muscle fatigue compared to vehicle-fed mice. The movement deficit can be due to the loss of dopaminergic neuronal function in the basal ganglia. Therefore, we tested the levels of tyrosine hydroxylase (TH) enzyme in the striatal tissue of both vehicle- and MHY-fed mice (Supplementary Fig. 2A, B). The dissection strategy was previously described [17]. The result demonstrated that there was no loss of TH in MHY-fed groups, nullifying the role of dopaminergic neuronal loss in movement impairment. While monitoring mTOR activation, our immunoblot results revealed that 2 weeks of MHY feeding significantly upregulated the level of Serine 2448-phosphorylated mTOR (Fig. 1K (i and ii)), whereas no change was observed in the total level of mTOR and Raptor, an essential factor of active mTOR complex 1. Moreover, our IB results indicated that the activation of mTOR was accompanied by the upregulation of S355-phosphorylated ATG13 (Fig. 1L (i and ii)) without altering the level of total ATG13. IB results were normalized with β-actin as a loading control.

Functionally active ATG13 forms a complex with ULK1, ATG101, and FIP200 at the early stage of autophagy [20]. Therefore, to explore the inactivation of ATG13, next, we monitored the formation of a complex between ATG13 and ULK1. To evaluate that, HEK293T cells were co-transfected with FLAG-ATG13 and HA-ULK1. Autophagy was induced following 24 h of starvation under serum-free conditions. Different doses of MHY1485 were added in these cells for 2 h before IP, followed by IB analyses. Interestingly, IP with HA followed by IB with FLAG and IP with FLAG following IB with HA indicated that 5 µM of MHY significantly impaired the formation of ATG13 and ULK1 complex after 2 h of starvation (Supplementary Fig. 3A), confirming the direct role of MHY1485 in the inactivation of ATG13.

A reduction in the number of autophagosomes does not necessarily indicate the impairment of autophagy. Induction of lysosomal function causing increased turnover of autophagosomes also displayed less numbers of autophagosomes. Therefore, next, we wanted to assess if the MHY 1485-mediated inactivation of ATG13 impaired the autophagy process [2], sparing lysosomal function. To test that, HEK293T cells, pre-transfected with eGFP-tagged LC3 (egfp-lc3) plasmid, were serum-starved for 24 h followed by 2 h of treatment with 5 µM MHY1485. Thirty minutes before plate-reading, cells were treated with 50 nM of LysoTracker™ Red DND-99 (Ex: Em = 577 nm/590 nm) and incubated at 37 °C. Accordingly, MHY1485 significantly inhibited the number of autophagosomes, as indicated by the reduced GFP signal (Supplementary Fig. 3B). However, there is no change in the lysotracker signal across different treatment groups (Supplementary Fig. 3C), suggesting that MHY1485 inhibits the formation of autophagosomes but does not alter the lysosomal function or lysosomal biogenesis. To further substantiate this, we performed fluorescence imaging of these HEK293T cells. Our results indicated that there was an induced autophagy process in starving conditions. However, 5 µM of MHY strongly inhibited the numbers of eGFP-LC3-ir autophagosomes but not lysotracker-ir lysosomes (Supplementary Fig. 3D). The total number of lysosomes remained the same. Nevertheless, the LC3 immunoblot analyses indicated that the serum starving induced the expression of LC3-II in HEK293T cells, whereas 5 µM MHY shifted the upregulation of the LC3-II isoform, indicating the impairment of the autophagy process (Supplementary Fig. 3E, F). Next, we assessed the cytotoxicity of MHY1485 by LDH

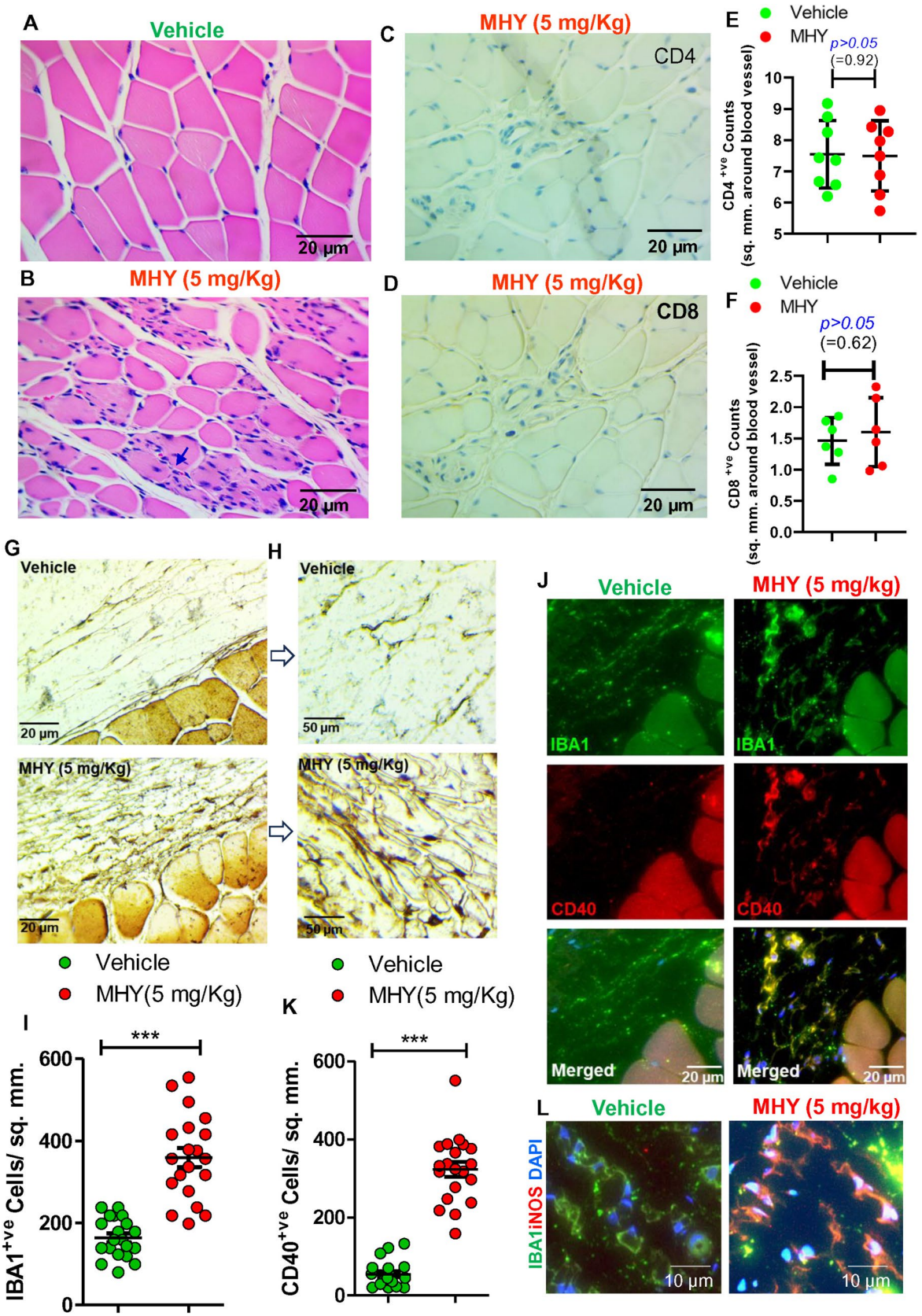
A
Vehicle
20 µm
B
MHY (5 mg/Kg)
20 µm
C
MHY (5 mg/Kg)
CD4
20 µm
D
MHY (5 mg/Kg)
CD8
20 µm
E
Vehicle
MHY
p>0.05
(=0.92)
CD4+ve Counts (sq. mm. around blood vessel)
F
Vehicle
MHY
p>0.05
(=0.62)
CD8+ve Counts (sq. mm. around blood vessel)
G
Vehicle
20 µm
MHY (5 mg/Kg)
20 µm
H
Vehicle
50 µm
MHY (5 mg/Kg)
50 µm
Vehicle
MHY(5 mg/Kg)
I
***
IBA1+ve Cells/ sq. mm.
Vehicle
MHY(5 mg/Kg)
K
***
CD40+ve Cells/ sq. mm.
J
Vehicle
MHY (5 mg/kg)
IBA1
IBA1
CD40
CD40
Merged
20 µm
Merged
20 µm
L
Vehicle
MHY (5 mg/kg)
IBA1iNOS DAPI
10 µm
10 µm

◂**Fig. 2** MHY1485 stimulates the infiltration and activation of M1 macrophage (M1Mφ) in muscle tissue. H&E staining in biceps muscle tissue of **A** vehicle and **B** MHY1485-fed mice (5 mg/kg). The infiltration of mononuclear cells (blue dots) was visible after 2 weeks of gavaging with MHY-1485 (alternative days at a dose of 5 mg/kg; $n = 8$/group). DAB immunostaining of serial Sects. (5 µm gap) by **C** CD4 and **D** CD8 antibodies demonstrated that these mononuclear cells were neither CD4-ir nor CD8-ir T cells. **E** and **F** are quantitative estimations of CD4- and CD8-ir cells, respectively. The quantification is done per 1 sq. mm parenchyma around blood vessels ($n = 5$/group). A total of 6 and 8 independent images per group were included for the quantifications of CD4 and CD8-ir cells, respectively. A non-parametric Mann–Whitney test was performed, and the resultant *p*-values were included on the histograms. IBA1 staining by DAB method in **G** vehicle- and **H** MHY-fed mice. **I** Quantification analyses of IBA1-ir cells were performed in 20 images (2 images from $n = 10$/group) in ImageJ software and plotted as dotted histograms in GraphPad Prism software. **J** Dual IF staining of IBA1 (green) and M1 Mφ marker CD40 (red) followed by **K** the quantification of CD40-ir cells were performed (total 20 images from two images in $n = 10$/group). Unpaired *t*-tests were performed to test the significance of means between groups. $^{***}p < 0.0001$ vs. vehicle as confirmed by parametric unpaired *t*-test. **L** Representative image of dual immunostaining of IBA1 and iNOS in the vehicle (left) and MHY-fed mice. Results are confirmed after three independent experiments

assay. We observed that 5 µM of MHY did not induce any apoptotic signals in HEK293T cells, nullifying the possibility of cell death as a confounding error; however, higher doses with more than 10 µM concentration induced LDH release (Supplementary Fig. 3G).

Since the activation of mTOR followed by ATG13 phosphorylation impairs the formation of autophagosome, resulting in autophagy impairment, next, we performed immunohistochemistry analysis of WDFY3 protein, an essential marker of the autophagosome, in the muscle tissue of vehicle- (Fig. 1M (i)) and 5 mg/kg MHY (Fig. 1M (ii))-fed mice ($n = 5$ per group). Accordingly, we observed that MHY-feeding significantly attenuated the numbers of WDFY3-immunoreactive autophagosomes compared to the vehicle group (Supplementary Fig. 4), suggesting that the chronic activation of mTOR followed by ATG13 phosphorylation impairs the formation of autophagosomes and inhibits the autophagy process.

Collectively, our results suggest that oral gavaging of MHY1485 stimulated chronic activation of mTOR following the phosphorylation of ATG13, impairment of autophagy in muscle, and induction of significant muscle fatigue in B6 mice.

Oral administration of MHY1485 stimulated infiltration and activation of M1 macrophages in muscle tissue

Next, we wanted to study how the chronic activation of mTOR following autophagy impairment contributed to muscle pathology in female B6 mice. While examining the morphology of WDFY3-ir bodies closely (inset; Fig. 1M (i and ii)), hematoxylin-stained cells were found to be surrounded by autophagosomes in muscle parenchyma. These cells are morphologically similar to macrophages. Accordingly, we performed a dual immunostaining of macrophage marker IBA1 together with WDFY3 in vehicle- and MHY-fed mice (Supplementary Fig. 5A). Interestingly, we observed that the autophagy process was highly operative in muscle infiltrating macrophages (Fig. 1N) in vehicle-fed mice, which was strongly attenuated in muscle tissue of MHY-fed mice (Supplementary Fig. 5A). Interestingly, our correlation study (Supplementary Fig. 5B) further corroborated that there was a strong negative correlation between IBA1-ir cells and WDFY3-ir autophagosomes in skeletal muscle tissue, suggesting the autophagy impairment could play an essential role in the activation and infiltration of macrophage in muscle tissue.

Autophagy impairment is known to exacerbate inflammation in chronic inflammatory [21–23] and autoimmune diseases [24, 25]. Therefore, next, we wanted to explore if chronic mTOR activation resulting in autophagy impairment augmented inflammation in skeletal muscle tissue. At first, our hematoxylin and eosin (H&E) staining in biceps muscle tissue displayed that there was a severe infiltration of mononuclear cells in the muscle parenchyma of MHY-fed (Fig. 2B) but not vehicle-fed (Fig. 2A) B6 female mice, indicating the potential role of chronic mTOR activation in the inflammatory mononucleosis in skeletal muscle tissue. However, DAB immunostaining of CD4 (Fig. 2C) and CD8 (Fig. 2D) in serial sections of muscle tissue followed by quantification analyses (Fig. 2E, F) revealed that neither $CD4^{+ve}$ nor $CD8^{+ve}$ T cells were found to be infiltrated in muscle parenchyma through the surrounding blood vessel. Interestingly, DAB immunostaining of IBA1, a marker protein of macrophage (Mφ), in the muscle tissue (Fig. 2G, H) followed by a quantification study (Fig. 2I) revealed that these infiltrated mononuclear cells were primarily macrophages. Moreover, a dual IF analysis of CD40, the surface marker of inflammatory the M1 subtype of Mφ, along with pan-Mφ marker IBA1 (Fig. 2J) followed by a quantification (Fig. 2K) study revealed that 2 weeks of MHY-feeding strongly upregulated the expression of M1Mφ marker CD40, suggesting that the chronic activation of mTOR induced the infiltration of M1Mφ cells. Dual IF staining of IBA1 with another Mφ-derived inflammatory marker iNOS (Fig. 2L) displayed an upregulated expression of iNOS in the MHY-fed group compared to vehicle-fed groups, further suggesting that these cells were truly inflammatory M1Mφ.

Next, we were interested in studying how these infiltrated M1Mφ cells elicited inflammatory changes in muscle cells. At first, we adopted Bielschowsky's silver staining procedure to monitor the myelin integrity in muscle-serving nerve fibers. The horizontally sectioned muscle fibers were

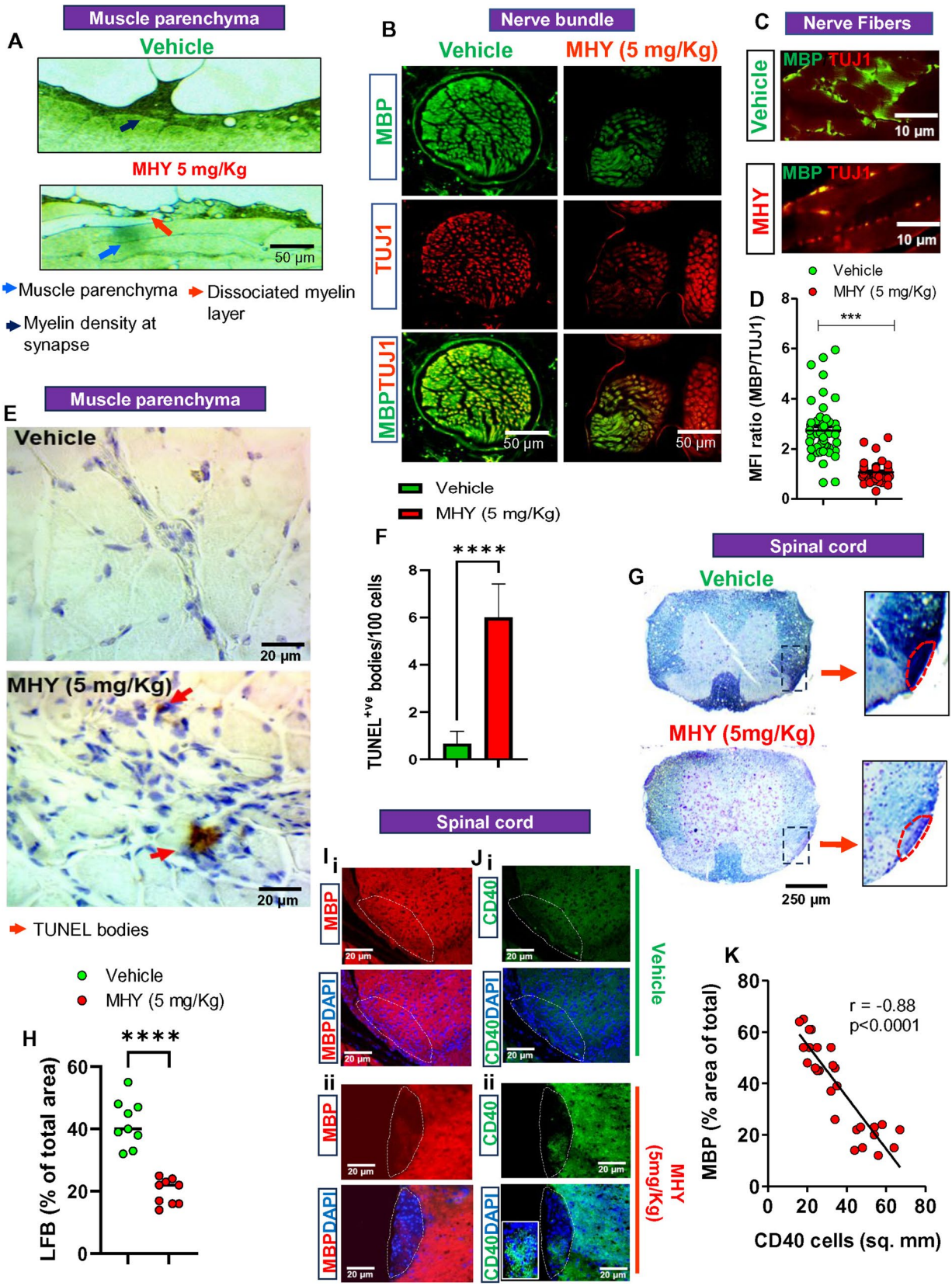
A
Muscle parenchyma
Vehicle
MHY 5 mg/Kg
50 µm
Muscle parenchyma
Dissociated myelin layer
Myelin density at synapse
B
Nerve bundle
Vehicle
MHY (5 mg/Kg)
MBP
TUJ1
MBPTUJ1
50 µm
C
Nerve Fibers
Vehicle
MHY
MBP TUJ1
10 µm
D
Vehicle
MHY (5 mg/Kg)
***
MFI ratio (MBP/TUJ1)
E
Muscle parenchyma
Vehicle
MHY (5 mg/Kg)
20 µm
TUNEL bodies
F
****
TUNEL+ve bodies/100 cells
G
Spinal cord
Vehicle
MHY (5mg/Kg)
250 µm
H
****
LFB (% of total area)
I
Spinal cord
MBP
MBPDAPI
J
CD40
CD40DAPI
K
r = -0.88
p<0.0001
MBP (% area of total)
CD40 cells (sq. mm)

◂**Fig. 3** MHY1485 augments demyelinating response in muscle and spinal cord. **A** Bielschowsky's silver staining of nerve fibers in horizontally sectioned biceps muscle tissue exhibits the loss of myelin integrity (blue arrow) in MHY-fed mice ($n=5$/group). **B** Dual IF analyses of myelin marker MBP and axonal marker TUJ-1 were performed in muscle-serving nerve bundles of the vehicle and SIM-fed mice. Transverse (dorsoventral) sectioning of the biceps muscle was performed to expose the nerve bundle. **C** Horizontal (anteroposterior axis) sectioning of muscle tissue followed by dual IF staining demonstrated a lateral view of MBP (green) and TUJ-1 (red) stained nerve fibers serving skeletal muscle (biceps) tissue. **D** MFI (mean fluorescence intensity) was calculated as described in the method section. Briefly, 10 nerve bundles were randomly selected from 5 different images with a total of 50 selections per group. MFI was calculated in the green channel for MBP and the red channel for TUJ1 in each nerve fiber. After that, the ratio was measured and plotted as a scatter histogram. An unpaired *t*-test was performed to test the significance of the mean between groups that resulted in $^{***}p<0.005$ versus control. **E** TUNEL staining followed by **F** quantification studies indicate that there was moderate but significant cell loss in MHY-fed muscle tissue. $^{****}p<0.0001$ versus vehicle as indicated by a non-parametric Mann–Whitney *U* test (24 images were assessed from $n=5$/group). **G** Luxol Fast Blue (LFB) staining exhibits the loss of myelin in the ventral horn of the lumbar spinal cord tissue of MHY-fed (lower panel), but not vehicle-fed (upper panel) mice. The demyelinating region was magnified and shown *inset*. **H** Eight LFB-stained spinal cord tissue were randomly selected per group followed by measuring the area of the entire image and that of only LFB-ir region in the area measuring tool of CaptaVision + (Accu-scope INC.) software. The result was shown by a dot histogram plot. Mann–Whitney *U* test revealed $^{****}p<0.0001$ versus control in 9 spinal cord images collected from $n=5$ mice/group. **I** IF staining of myelin marker MBP (red) in the demyelinated ventral horn of the lumbar spinal cord of vehicle- (upper panel) and MHY- (lower panel) fed mice. The magnified images were shown *inset*. **J** IF analysis of M1 Mφ marker CD40 (green) in the demyelinated ventral region of the spinal cord in MHY-fed mice. Nuclei were stained with DAPI (blue). **K** A parametric Pearson correlation analysis was shown in a scatter plot between the % of MBP-ir area of the spinal cord (*Y*-axis) and CD40-ir cells (*X*-axis) in 27 spinal cord images. Results are confirmed after three independent experiments in $n=5$ mice per group

stained with 10% silver nitrate as discussed in the method section. The high-resolution images of nerve terminals were visualized under a phase contrast microscope and recorded at × 100 magnification (Fig. 3A). The myelin layers in vehicle-fed mice were observed to strongly adhere to muscle parenchyma. However, we observed that the oral administration of MHY1485 significantly compromised the integrity of myelin layers on muscle fibers, as indicated with lightly colored, disintegrated, and vacuolated myelin layers on muscle parenchyma. Next, a dual immunostaining method of myelin marker MBP and axonal marker TUJ1 was adopted to evaluate the myelin integrity (Fig. 3B). The presence of myelin layers as indicated with strong MBP staining was expected to mask axons as indicated with less TUJ1 signal. Accordingly, the dual immunostaining of MBP and TUJ1 in transversely sectioned muscle tissue indicated that the integrity of myelin layers in the muscle-serving nerve terminal of the MHY-fed group was severely compromised, and as a result, the TUJ1-ir axons were exposed, whereas MBP-ir myelin layers remained tightly wrapped around axonal fibers of vehicle-fed mice. The integrity of myelinated nerve fibers was further evaluated in horizontally sectioned muscle fibers by similar dual immunostaining of MBP and TUJ1 (Fig. 3C), which indicated that the oral administration of MHY, but not the vehicle, significantly damaged the myelin integrity. Moreover, the quantitative estimation of the ratio between the MFI of MBP and that of TUJ1 (Fig. 3D) confirmed that indeed there was a strong demyelinating response in the muscle fibers after chronic mTOR activation. Next, we evaluated if the chronic administration of MHY1485 caused apoptosis in muscle cells. Interestingly, our TUNEL staining identified the $TUNEL^{+ve}$ apoptotic signals (Fig. 3E) in the muscle cells around the blood vessel, where strong infiltration of mononuclear cells was observed. The result was further confirmed by quantification analysis (Fig. 3F). Skeletal muscle-serving efferent nerve fibers originated at the ventral horn of the spinal cord. Therefore, next, we were interested in exploring the myelin integrity in the ventral part of the spinal cord. Accordingly. LFB staining in the dorsoventrally sectioned spinal cord tissue (Fig. 3G) indicated a strong reduction of myelin staining, particularly in the ventral spinal tissue of MHY-fed mice. Accordingly, the quantitative estimation was performed to measure the volume of the LFB-stained region compared to the total volume of spinal cord tissue on a percent scale, and the resultant analyses further demonstrated that chronic MHY feeding truly generated a demyelinating response in the ventral horn region of the spinal cord (Fig. 3H). The demyelinating response in spinal cord tissue was further evaluated by IF staining with MBP (Fig. 3I). To study the role of M1Mφ cells (CNS subtype is M1 microglia) in spinal cord demyelination, a CD40 immunostaining analysis was adopted. Interestingly, our analysis identified that there was an infiltration of CD40-ir M1Mφ cells (Fig. 3J) in the demyelinated spinal cord tissue. Nevertheless, a parametric correlation analysis between the MBP-ir area of the spinal cord and the number of CD40-ir cells (Fig. 3K) further revealed that MHY feeding caused the demyelinating response in the spinal cord following the infiltration of activated M1Mφ cells. Collectively, our results suggest that the severe infiltration of M1Mφ causing the demyelinating response in muscle-serving nerves resulted in the apoptosis of muscle cells.

Chronic mTOR activation is required for the expressions of IL-6 and RANTES via activation of STAT3 in muscle tissue

So far, our results suggest that chronic administration of MHY1485 following mTOR activation recruited inflammatory M1Mϕ cells and implemented a demyelinating response

in muscle tissue. Next, we wanted to explore the effect of chronic mTOR activation on the expressions of inflammatory cytokines in these cell types. First, a cytokine array of 40 different cytokines revealed that 5 µM MHY-1485, but not solvent control (DMSO), significantly induced the expressions of IL6 and RANTES (Fig. 4A), but not other inflammatory cytokines such as IL-1β, TNFα, IL12, or IFN-γ in human C20 microglial cells. Upregulations of inflammatory chemokines such as MCP-1, MIP-1α, and eotaxin were also not observed. The result was further confirmed

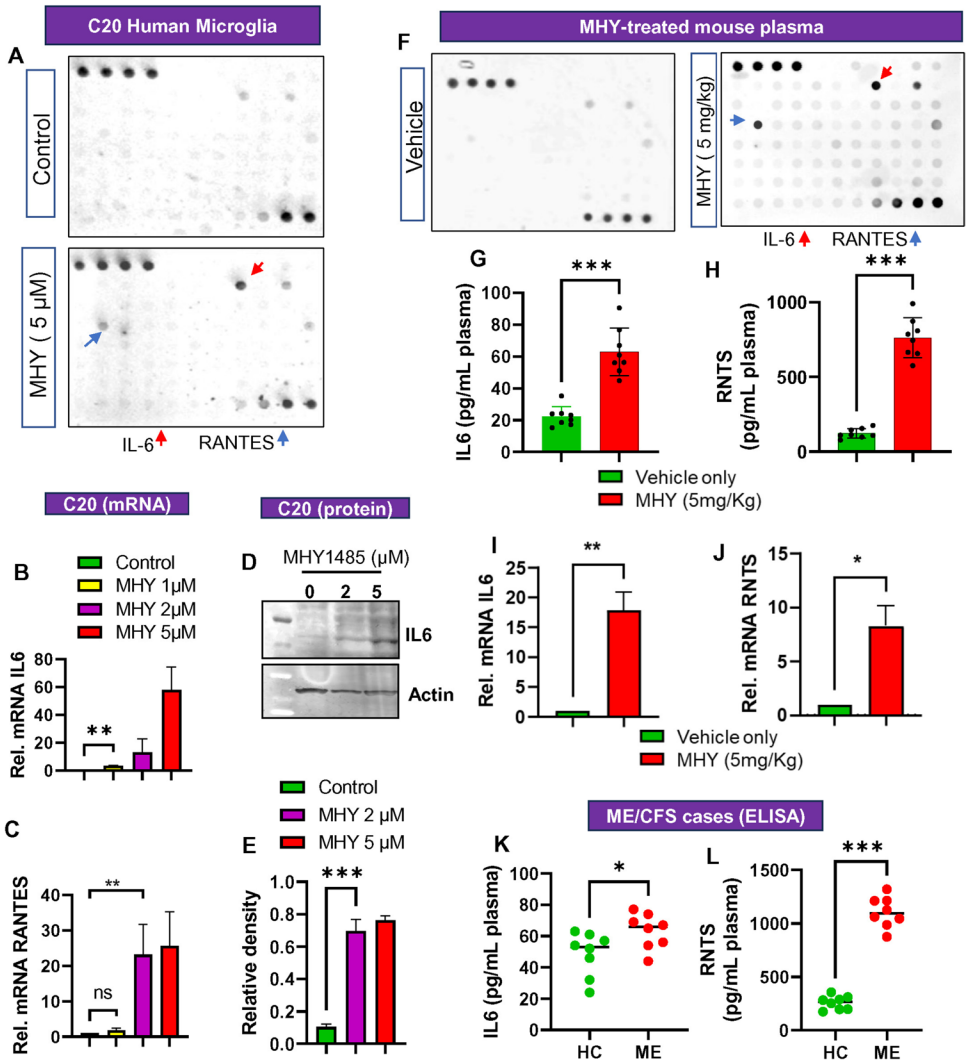

Fig. 4 MHY1485 upregulates IL6 and RANTES. **A** An antibody array of 40 inflammatory cytokines (RayBiotech) was performed in the supernatants of C20 human microglial cells treated with 5 µM of MHY1485 for 48 h. Control sup was collected from microglia treated with DMSO for 48 h. The red arrow shows the IL6 expression, whereas the blue arrow indicates the RANTES expression. **B** Realtime mRNA expressions of IL6 were monitored in microglia treated with 1, 2, and 5 µM of MHY for 5 h under serum-free conditions. $^{**}p<0.01$ versus control as measured with the Mann–Whitney non-parametric test. **C** Realtime mRNA expressions of RANTES were monitored in human microglial cells treated with 1, 2, and 5 µM of MHY1485 for 5 h under serum-free conditions. $^{**}p<0.01$ versus control as measured with the Mann–Whitney test. **D** Immunoblot analysis of IL6 (~20 kDa) was performed in human microglial cells after treating increasing doses of MHY1485 for 24 h. The resultant expression was normalized with respective β-actin expressions followed by analyzing **E** relative density. $^{**}p<0.01$ versus control (Mann–Whitney test). **F** At 14 days, after the last dose of MHY1485 feeding blood collection was carried out via cardiac puncture method, serum was isolated in heparin tube, and then performed a similar antibody array method of 40 inflammatory cytokines. Red and blue arrows indicate IL6 and RANTES expressions, respectively. ELISA analyses of **G** IL6 and **H** RANTES in the serum samples were performed ($n=8$/group). Non-parametric Mann–Whitney test represents $^{***}p<0.005$ ($=0.0002$) versus vehicle. Realtime mRNA expressions of **I** IL6 and **J** RANTES were performed in muscle tissue of vehicle and MHY-fed mice ($n=5$ per group). The non-parametric Mann–Whitney tests represent $^{**}p<0.01$ and $^{*}p<0.05$ versus vehicle. Results are mean ± SEM of three different experiments. **K** IL6 and **L** RANTES concentrations were also measured by quantitative ELISA methods in sera of $n=8$ healthy and age-matched $n=8$ ME/CFS patients. Mann–Whitney tests represent $^{*}p<0.05$ ($=0.0407$) and $^{***}p<0.005$ ($=0.0002$) versus the control group. Results are mean ± SEM of three different experiments

by quantitative real-time PCR analyses of IL6 (Fig. 4B) and RANTES (Fig. 4C) and IB of IL6 (Fig. 4D), followed by relative densitometric quantification (Fig. 4E). Next, a similar cytokine array in the serum samples of mice dosed with 5 mg/kg bwt MHY1485 resulted in similar upregulations in both IL6 and RANTES but not other cytokines (Fig. 4F). Subsequent ELISA analyses of IL6 (Fig. 4G) and RANTES (Fig. 4H) in the plasma of MHY1485-treated mice ($n=5$) further confirmed that both cytokines were strongly upregulated after 2 weeks of feeding with 5 mg/kg bwt MHY1485. Apart from myeloid-lineage macrophage or microglia cells, both these cytokines are also found to be profusely expressed in muscle cells and therefore called myokines. Interestingly, mRNA analyses revealed that upon 2 weeks of feeding with 5 mg/kg bwt MHY1485, gene expressions of IL6 (Fig. 4I) and RANTES (Fig. 4J) were significantly upregulated in muscle tissue. To explore the clinical relevance of these findings, plasma samples of eight control and eight age-matched ME/CFS patients were analyzed for ELISA analyses of IL6 (Fig. 4K) and RANTES (Fig. 4L). Interestingly, strong elevations of IL6 and RANTES were observed in the plasma samples of ME/CFS patients, suggesting that MHY1485-induced upregulations of IL6 and RANTES are pathologically relevant to ME/CFS. To explore the direct role of mTOR in the upregulations of IL6 and RANTES, the de novo expression of mTOR was attenuated by mTOR siRNA (Supplementary Fig. 6A, B) in MHY-treated C20 microglial cells, followed by IL6 (Supplementary Fig. 6C) and RANTES (Supplementary Fig. 6D) protein expressions. MHY-1485 failed to upregulate IL6 and RANTES once the expression of mTOR was attenuated in microglial cells, suggesting the direct role of mTOR in the upregulations of IL6 and RANTES in microglial cells.

Next, we were interested in exploring how MHY1485 stimulated the expressions of IL6 and RANTES. Upon activation, mTOR activates STAT3 via phosphorylation at its Serine 727 and Tyrosine 705 residues [26, 27]. To test these possibilities, human microglial cells were stimulated with 1, 2, and 5 μM of MHY1485 for 2 h, then fractionated for nuclear extract, and finally analyzed for IB. Interestingly, MHY1485 dose-dependently induced the phosphorylation and subsequent nuclear translocation of Y705P STAT3, but not S727P STAT3 (Fig. 5A). The result was normalized with H3 histone. This result indicates the possible role of MHY1485-induced Y705 phosphorylation of STAT3 in the transcriptional regulations of IL6 and RANTES. To further confirm, these nuclear extracts were probed with an oligonucleotide probe of STAT3 and run for an EMSA gel-shift assay. Based on that result, MHY1485 dose-dependently induced the DNA-binding of STAT3 (Fig. 5B), suggesting that MHY1485 induced the transcriptional activity of STAT3. Interestingly, subsequent promoter analysis of IL6 at chromosome 7 detected a consensus STAT3 response element (Fig. 5C). A chromatin immunoprecipitation (ChIP) by STAT3 antibody study followed by real-time PCR with IL6 promoter-specific primers indicated that MHY1485 directly induced the recruitment of STAT3 at the IL6 promoter (Fig. 5D, E). The specificity of ChIP was validated by the IP with IgG (Fig. 5F). Similarly, a canonical STAT3 binding site was also observed in the RANTES promoter (Fig. 5G), and the subsequent ChIP analyses revealed that upon MHY treatment, there was an augmented recruitment of STAT3 (Fig. 5H, I) in the RANTES promoter of C20 microglial cells. The specificity of STAT3 recruitment was further confirmed by the negative PCR data in the IgG-pulled fraction (Fig. 5J). To evaluate the role of STAT3 in inducing the transcription of IL6, next, we performed a GFP reporter assay, in which IL6 promoter with STAT3 response element was cloned upstream of GFP reporter (p^{wtIL6}). The GFP construct was then transfected to human microglial cells, followed by treatment with different doses of MH1485 for 5 h. Interestingly, increasing doses of MHY1485 stimulated GFP reporter activity (Fig. 5K), as shown by a fluorometric assay measured with Ex: Em = 480 nm/535 nm signal ratio. To further validate the result, we performed a site-directed mutagenesis of the STAT3 response element at the IL6 promoter ($p^{\Delta IL6}$) followed by the transfection in human microglial cells (Fig. 5L). Subsequent fluorimetric analysis revealed that increasing doses of MHY1485 were unable to induce the GFP reporter activity once cells were transfected with *the* $p^{\Delta IL6}$ promoter. While exploring the effect of MHY1485 feeding on the activation of STAT3 in skeletal muscle, our DAB staining indicated that the oral administration of MHY significantly stimulated the levels of Y705PSTAT3 (Fig. 5M) in the epithelium of biceps muscle tissue compared to control. Further analysis revealed that these Y705PSTAT3-ir cells were mostly IBA1-ir macrophages (Fig. 5N). Collectively, our results suggest that the chronic mTOR activation followed by the STAT3 phosphorylation at its Tyr 705 is critical for the upregulation of IL6 and RANTES in infiltrated M1Mϕ cells, leading to the chronic inflammation and demyelinating response in muscle tissue.

Suppression of ATG13 in ATG13 repressor (Tg-ATG13) mice showed severe but transient post-exertional fatigue

A pathological hallmark of chronic fatigue syndrome is post-exertional fatigue. Does chronic mTOR activation feeding exacerbate muscle fatigue after treadmill exercise? To answer that question, we performed a single-session treadmill exercise trial in vehicle- (Fig. 6A) and MHY1485 (5 mg/kg)-fed (Fig. 6B) mice. Mice were fed with MHY1485 (5 mg/kg) on alternative days for 2 weeks, rested for 1 week, and then subjected to treadmill exercise for monitoring the post-exertional fatigue. The overall movement was monitored 1 day before, immediately after, and 2 days after treadmill exercise in an ANY-maze infrared sensor-controlled

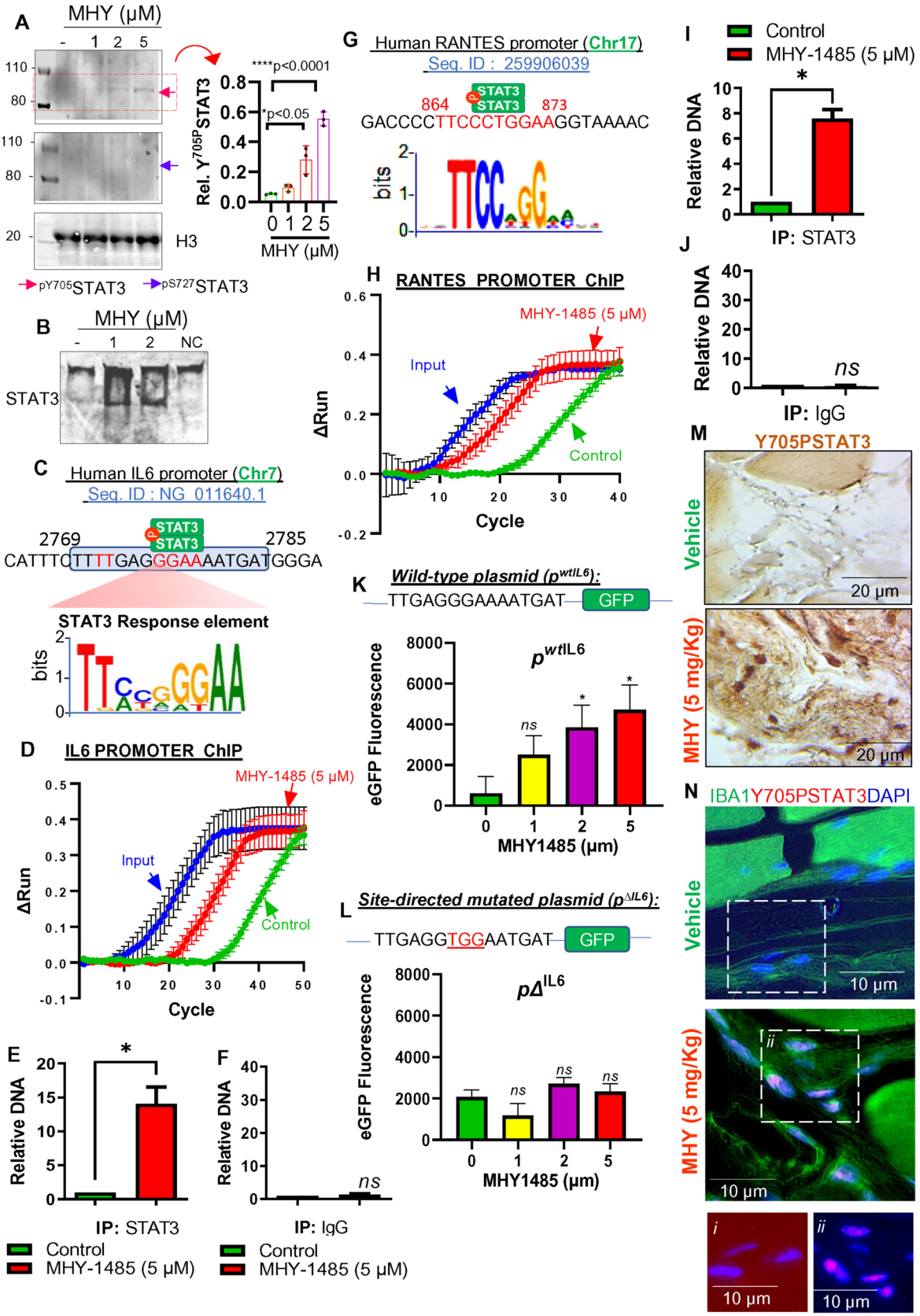
A
MHY (μM)
- 1 2 5
110
80
110
80
20
H3
pY705STAT3
pS727STAT3
Rel. Y705PSTAT3
****p<0.0001
*p<0.05
0 1 2 5
MHY (μM)
B
MHY (μM)
- 1 2 NC
STAT3
C
Human IL6 promoter (Chr7)
Seq. ID : NG_011640.1
2769
2785
CATTTCTTTTGAGGGAAAATGATGGGA
STAT3
STAT3
STAT3 Response element
bits
D
IL6 PROMOTER ChIP
MHY-1485 (5 μM)
Input
Control
ΔRun
Cycle
E
Relative DNA
IP: STAT3
Control
MHY-1485 (5 μM)
F
Relative DNA
IP: IgG
ns
Control
MHY-1485 (5 μM)
G
Human RANTES promoter (Chr17)
Seq. ID : 259906039
864
873
GACCCCTTCCCTGGAAGGTAAAAC
STAT3
STAT3
bits
H
RANTES PROMOTER ChIP
MHY-1485 (5 μM)
Input
Control
ΔRun
Cycle
K
Wild-type plasmid (pwtIL6):
TTGAGGGAAAATGAT
GFP
pwtIL6
eGFP Fluorescence
MHY1485 (μm)
L
Site-directed mutated plasmid (pΔIL6):
TTGAGGTGGAATGAT
GFP
pΔIL6
eGFP Fluorescence
MHY1485 (μm)
I
Control
MHY-1485 (5 μM)
Relative DNA
IP: STAT3
J
Relative DNA
ns
IP: IgG
M
Y705PSTAT3
Vehicle
MHY (5 mg/Kg)
20 μm
N
IBA1Y705PSTAT3DAPI
Vehicle
MHY (5 mg/Kg)
10 μm
i
ii

◂**Fig. 5** The essential role of STAT3 in MHY 1485-mediated expression of IL6 and RANTES. **A** Immunoblot analyses of mTOR with phosphorylated tyrosine 705 (pY705) and phosphorylated Serine727 (pS727) in the nuclear extracts of human C20 microglial cells treated with 1, 2, and 5 μM of MHY1485. Histone 3 (H3) immunoblot analysis was performed as a control. (*Inset*) Densitometric analyses were done in ImageJ followed by normalization with respective H3 bands. **B** EMSA analysis of STAT3 (probed with STAT3 oligonucleotide; Li-Cor Bioscience) in the nuclear extracts of human microglial cells treated with 1 and 2 μM MHY1485 (NC = negative control). The raw blot is shown in Supplementary Fig. 10. **C** The promoter analysis of the human IL6 promoter at chromosome 7 displays the detailed location and sequence of consensus STAT3 responsive element. **D** Chromatin immunoprecipitation (ChIP) analysis of STAT3- and IgG-pulled DNA (product length = 123 bp) surrounding STAT3 responsive element of IL6 promoter. Chromosomal DNA was isolated from blue = input; green = control; and red = 5 μM MHY1485-treated microglial cells, performed with ChIP, and the resultant real-time PCR amplification data suggests increased binding of STAT3 at IL6 promoter. Fold increases in **E** anti-STAT3- and **F** IgG-pulled down DNA were displayed after normalizing the Ct value of MHY-pulled down DNA with the Ct value of the input. $*p < 0.05$ versus control and ns = no significance. Results were mean ± SD of three different experiments. **G** Human RANTES promoter map at chromosome 17 with location and sequence. **H** Realtime PCR amplification of human RANTES promoter pulled down by anti-STAT3 antibody in human microglial cells treated with 5 μM MHY1485 (red). Control cells were treated with DMSO (green), and input (blue) was no antibody-treated group. Fold-increase of chromosomal DNA surrounding the STAT3-responsive element of the RANTES promoter was quantified after pulling down with **I** STAT3 antibody and **J** IgG. The result was further quantified with relative Ct analyses in (K) anti-STAT3 and (L) IgG-pulled DNA after normalizing with input Ct. $*p < 0.05$ versus control and ns = no significance. Results were mean ± SD after three different experiments. **K** GFP-reporter assay of wild-type IL6 promoter cloned at STAT3 response element tagged GFP at the N-terminus region (p^{wtIL6}). The promoter clone was transfected in HEK293T cells followed by stimulation with 1, 2, and 5 μM of MHY1485, and the resultant GFP signal was quantified with Ex: Em = 485 nm:535 nm. Results are mean ± SD of three different experiments. $*p < 0.05$ versus control and ns = no significance. **L** Site-directed mutagenesis of STAT3-response element of human IL6 promoter followed by the construction of a GFP reporter clone was performed. A dose-dependent effect of MHY1485 on the expression of GFP reporter was evaluated in HEK293T cells. ns = no significance. **M** DAB immunostaining of Y705PSTAT3 in skeletal muscle tissue (biceps muscle biopsies) of vehicle- and 5 mg/kg MHY1485-fed mice ($n = 5$/group). The representative image was derived from muscle epithelium. **N** Dual IF analysis of Y705PSTAT3 and macrophage-marker IBA1 in epithelial tissue of vehicle- and MHY-fed mice ($n = 5$/per group). Insets are magnified images of respective enclosed areas. Nuclei were stained with DAPI

open-field arena. Animals were subjected to running on the treadmill at a speed of 14 rpm for 15 min following 1 min of acclimatization at a speed of 8 rpm. The baseline movement recorded one day before the treadmill exercise was found to be moderate but significantly diminished (Supplementary Fig. 7A) in MHY-fed mice (Fig. 6B; first row) compared to vehicle-fed mice ($n = 5$ per group) (Fig. 6A; first row). The treadmill exercise implemented acute but temporary fatigue immediately after treadmill exercise in both vehicles- (Fig. 6A; second row) and MHY-fed (Fig. 6B; second row) groups, as shown by track-plot analyses. However, quantitative measurement of average speed (Supplementary Fig. 7A) indicated that MHY-fed mice displayed severe acute fatigue with significantly less physical movement compared to vehicle-fed mice. Interestingly, 2 days of complete rest completely recovered the vehicle-fed mice (Fig. 6A; third row). However, MHY-fed mice continued to display severe impairment of physical movement even after 2 days of complete rest, as indicated by our track-plot analysis (Fig. 6B; third row), followed by quantitative measurement of average speed (Supplementary Fig. 7A) in the arena. Since our results indicate that the functional inactivation of ATG13 implements muscle fatigue, next we wanted to develop a unique transgenic mouse model to study the direct role of ATG13 in post-exertional fatigue. Embryonic ablation of *the atg13* gene is lethal in the fetal stage. Therefore, we generated a knock-out first ATG13-repressor mouse (Tg-ATG13) in which a lacZ repressor element was inserted upstream of exon 5 of its *atg13* gene (Fig. 6C). The generated ATG13 strain was genotyped for the presence of a 499 bp long transgene (Fig. 6D). We also monitored the expression of the *atg13* gene by semiquantitative and real-time PCR (Supplementary Fig. 8A, B) to confirm the genetic suppression of the atg*13* gene in Tg-ATG13 mice. Interestingly, while recording the baseline movement, Tg-ATG13 mice displayed a significantly slow movement as monitored by a track-plot analysis (Fig. 6E; first row) followed by a quantitative analysis of average speed (Supplementary Fig. 7A). Accordingly, a single-session treadmill exercise implemented acute fatigue with significantly impaired gross movement activity, as shown by our track-plot analysis (Fig. 6E; second row). The result showed complete immobility or "crash" in 20% of Tg-ATG13 ($n = 2$ out of 5 mice) mice. Our track-plot analysis further demonstrated that 2 days of complete rest was unable to restore the baseline physical activity in Tg-ATG13 mice (Fig. 6E; third row). However, we did not see any changes in neurocognitive behavior in these animals as tested by Barnes maze analyses. Neither MHY-fed nor Tg-AG13 mice showed any impairment in spatial learning compared to NTG mice after a single session of treadmill exercise (Supplementary Fig. 7B, C). To understand the muscle fatigue of Tg-ATG13 mice at the molecular level, we performed EMG recording analyses in the biceps femoris muscle of 5 to 6-week-old non-transgenic (NTg) wild-type (Fig. 6F) and Tg-ATG13 (Fig. 6G) mice 1 day before, immediately after, and 2 days after treadmill exercise. The non-invasive ring electrode was attached, removed, and re-attached to the surface of the biceps muscle to record muscle waves during different time points without causing any physical discomfort to mice. Accordingly, the baseline muscle waves were calculated for both NTg and Tg-ATG13 mice 1 day before treadmill exercise. However, immediately after treadmill exercise, the recorded EMG for Tg-ATG13,

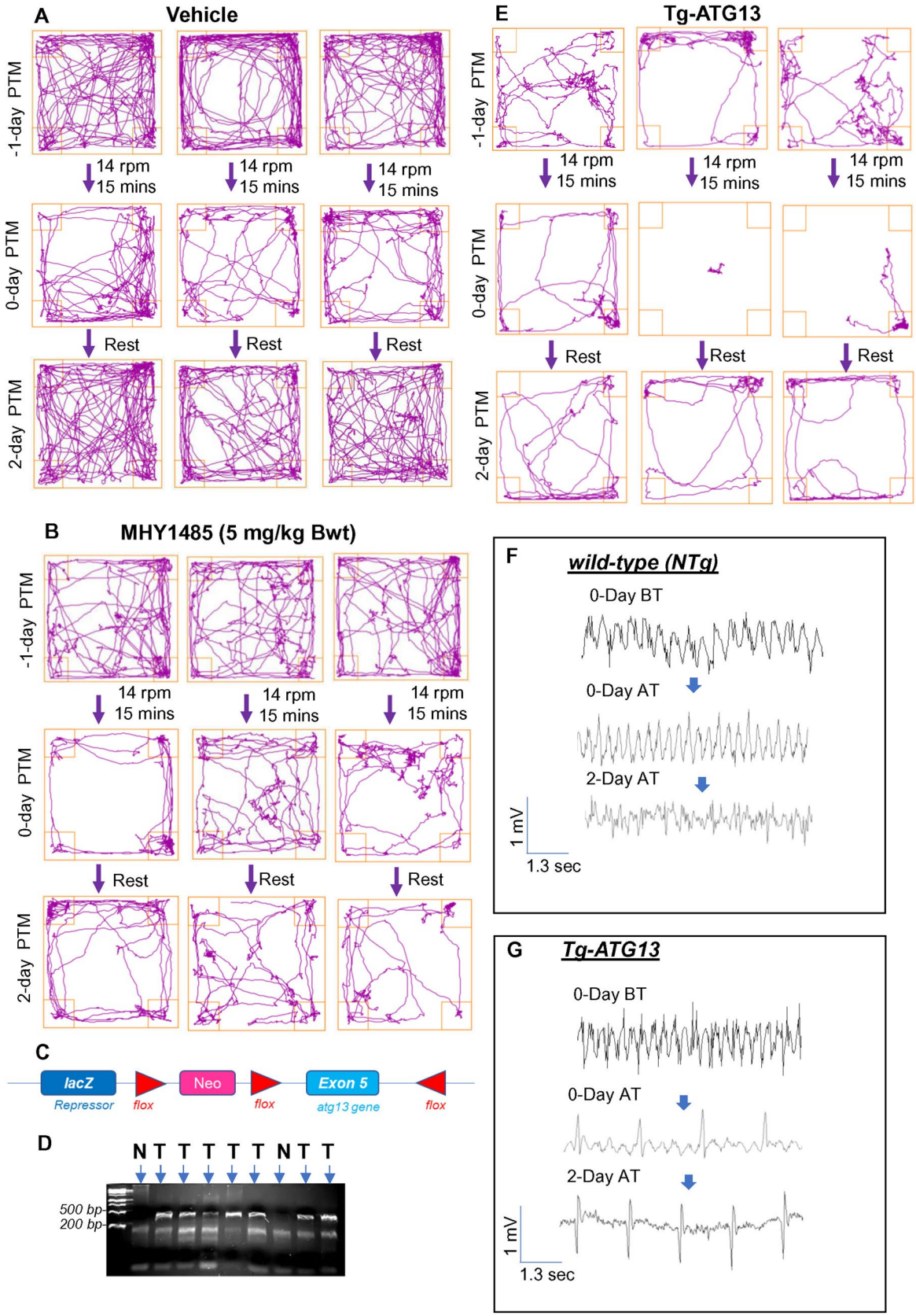
A
Vehicle
-1-day PTM
14 rpm
15 mins
0-day PTM
Rest
2-day PTM
E
Tg-ATG13
B
MHY1485 (5 mg/kg Bwt)
C
lacZ
Repressor
flox
Neo
Exon 5
atg13 gene
D
N T T T T T N T T
500 bp
200 bp
F
wild-type (NTg)
0-Day BT
0-Day AT
2-Day AT
1 mV
1.3 sec
G
Tg-ATG13

◂**Fig. 6** mTOR-ATG13 crosstalk in post-exertional fatigue. After 14 days of the vehicle and MHY1485 (5 mg/kg), gavaging, 5- to 6-week-old female B6 mice ($n=8$/ group) were subjected to treadmill running at a speed of 14 rpm for 15 min. Representative images ($n=3$/group) were open field gross movement of **A** vehicle and **B** MHY-fed 3- to 4-week-old female B6 mice ($n=8$) before, immediately after, and 2 days after treadmill exercise. **C** A schema of a genetic map for the generation of ATG13 suppressor mice (Tg-ATG13). A lacZ repressor cassette was inserted in front of crucial exon 5 of the *atg13* gene. **D** PCR strategy to genotype these mice to identify the transgene of 499 bp (T = transgenic; N = non-transgenic). **E** Five- to six-week-old female ATG13-KO ($n=8$) mice were subjected to a treadmill tolerance test at a speed of 14 rpm. The cut-off time limit is 15 min. The gross movement was monitored before, immediately after, and 2 days after treadmill exercise were recorded, and representative images for $n=3$ mice were displayed. EMG recordings in **F** wild-type littermate and **G** Tg-ATG13 mice before, 0 days after, and 2 days after treadmill exercise. Results are confirmed after three different experiments

but not NTg mice (Fig. 6F; second row), exhibited low-frequency muscle waves with periodic bursts (Fig. 6G; second row) characteristic of myokymia. Interestingly, these low-frequency myokymic muscle waves became more prominent and intense 2 days after post treadmill exercise (Fig. 6G; third row), suggesting that ATG13 ablation is critical in the development of post-exertional fatigue in mice.

Next, we wanted to study the molecular role of ATG13 in inducing muscle fatigue in the Tg-ATG13 mouse model. At first, WDFY3 staining (Fig. 7A) followed by a quantification study (Fig. 7B) revealed that there was a significant impairment of autophagy in Tg-ATG13, but not NTg, mice. While evaluating the inflammatory mononucleosis as a downstream event of autophagy impairment, a subsequent H&E staining revealed that there was a strong infiltration of blood-borne mononuclear cells in the vasculature and epithelial layers of muscle tissue in Tg-ATG13, but not NTg, mice (Fig. 7C), suggesting that the suppression of ATG13 may be involved in the induction of inflammation in the muscle tissue of Tg-ATG13 mice. Further characterization of these mononuclear cells by immunohistochemical analyses revealed that these cells were IBA1-ir macrophages (Fig. 7D). Moreover, a subsequent dual immunofluorescence study (Fig. 7E) followed by a quantification analysis (Fig. 7F) indicated that these IBA1-ir cells were also CD40-ir cells, suggesting that the suppression of ATG13 stimulated the induction and infiltration of M1Mϕ cells in the skeletal muscle tissue of Tg-ATG13 mice. Interestingly, a dual immunostaining analysis of IBA1 and Y705PSTAT3 indicated that there was a strong activation of STAT3 in these cells, and upon activation, Y705PSTAT3 was found to be translocated in nuclei (Fig. 7G) of these infiltrated M1Mφ cells, suggesting that Tg-ATG13 mice may display the potential inflammatory demyelination response in muscle tissue. Accordingly, we adopted Bielschowsky's silver staining procedure to identify myelin integrity in muscle tissue. In NTg mice, we observed normal dark-stained myelinated axonal fibers as indicated by the red arrowhead (Supplementary Fig. 9). However, similar staining indicated significantly less myelin as identified by thin dark lines in the muscle tissue of Ttg-ATG13 mice. Dual IF staining of MBP (green) and TUJ1 (red) in muscle-serving nerve bundles (Fig. 7H) showed that the MBP-ir myelin layer is tightly wrapped around TUJ1-ir axonal fibers in NTg mice, whereas the integrity of the myelin layer is compromised in the TUJ1-ir nerve bundle Tg-ATG13 mice. The loss of myelin integrity in Tg-ATG13 mice was further quantified (Fig. 7I) by measuring the correlation of MFI between MBP and TUJ1 ($n=5$ per group). Next, we were interested in exploring the myelin integrity in the muscle-serving efferent nerve fibers originating from the ventral horn of the spinal cord. Interestingly, the myelin staining by the LFB method (Fig. 7J) indicated that the myelin integrity was severely compromised in Tg-ATG13, but not NTg, mice.

Collectively, our current study highlights a novel signaling mechanism of muscle fatigue and post-exertional fatigue with the following cascade of events, including chronic mTOR activation, the inactivation of ATG13 followed by impairment of autophagy, induction of inflammatory mononucleosis, production of inflammatory IL6 and RANTES via STAT3 activation, and finally demyelination of muscle serving nerve fibers.

Discussion

Chemically induced chronic activation of mTOR induces muscle fatigue in young female mice

ME/CFS is a chronic multisystem disease characterized by extreme muscle fatigue, pain, and inflammation. One of the hallmark symptoms of this illness is post-exertional malaise (PEM), which is severe muscle fatigue and pain after physical or mental exercise. Until now, the molecular mechanism of PEM is poorly understood. Primary limitations that impede understanding molecular mechanisms are as follows: *First*, there is a shortage of sufficient post-mortem biospecimens such as the brain, spinal cord, and muscle tissue. *Second*, the disease is highly heterogeneous with unknown etiology. *Finally*, there is no disease-relevant animal model to study the molecular mechanism of PEM. In our current manuscript, we attempted to decipher the molecular mechanism of PEM by introducing a drug-induced mouse model in which the chronic activation of mTOR plays a critical role in inducing muscle fatigue and PEM-like symptoms. MHY1485, a pharmacological agonist of mTOR, was administered orally at 2, 5, and 10 mg/kg bwt doses to 3- to 4-week-old C57BL/6 mice on alternate days for 2 weeks. Starting from the 3rd dose, severe acute fatigue was observed predominantly in female mice. Nine out of 10 female mice displayed fatigue pathology, whereas 3 out of 10

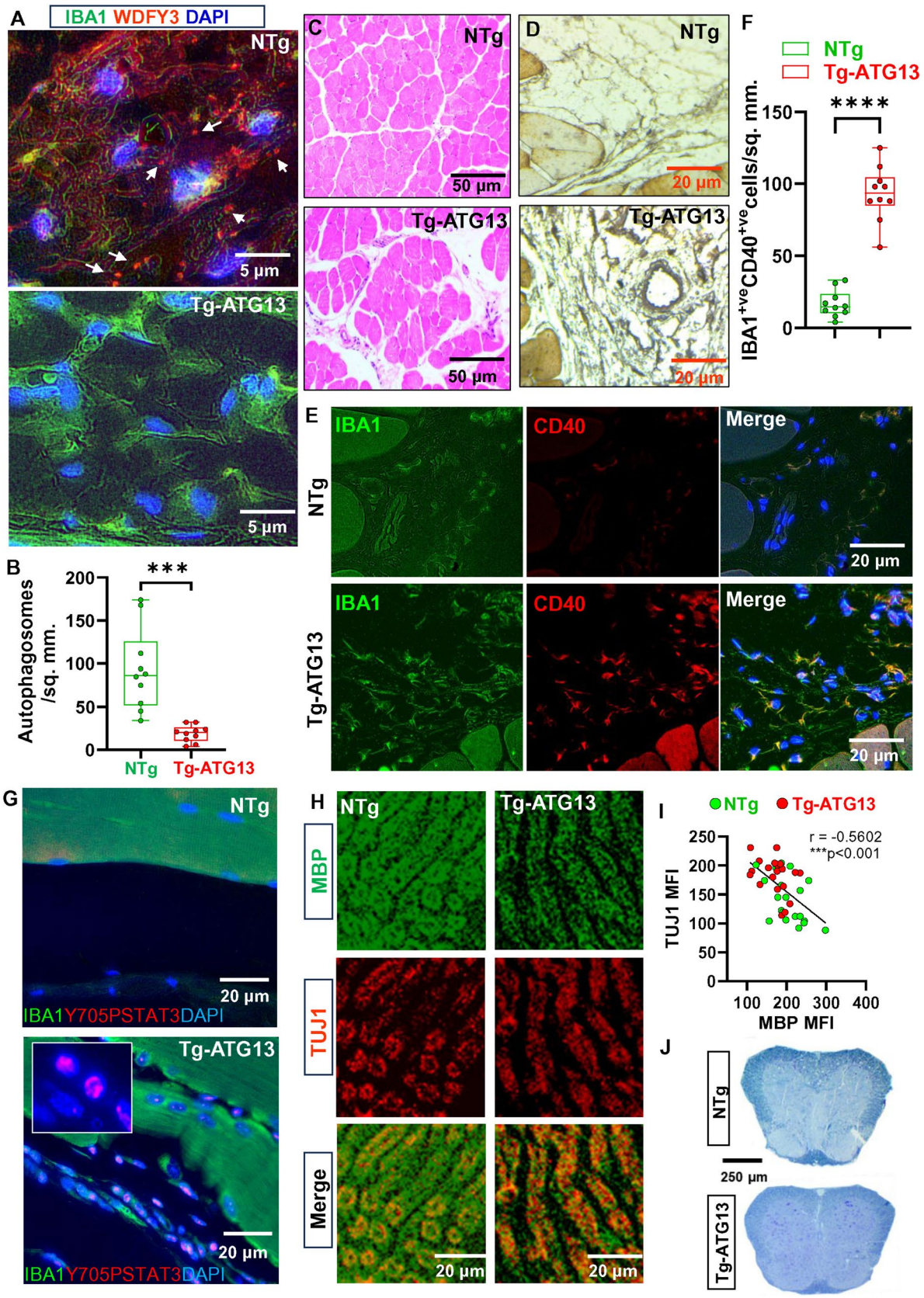
A
IBA1 WDFY3 DAPI
NTg
5 µm
Tg-ATG13
5 µm
B
***
Autophagosomes /sq. mm.
200
150
100
50
0
NTg
Tg-ATG13
C
NTg
50 µm
Tg-ATG13
50 µm
D
NTg
20 µm
Tg-ATG13
20 µm
E
IBA1
CD40
Merge
NTg
20 µm
IBA1
CD40
Merge
Tg-ATG13
20 µm
F
NTg
Tg-ATG13
****
IBA1+veCD40+ve cells/sq. mm.
150
100
50
0
G
NTg
20 µm
IBA1Y705PSTAT3DAPI
Tg-ATG13
20 µm
IBA1Y705PSTAT3DAPI
H
NTg
Tg-ATG13
MBP
TUJ1
Merge
20 µm
20 µm
I
NTg
Tg-ATG13
r = -0.5602
***p<0.001
TUJ1 MFI
250
200
150
100
50
0
100
200
300
400
MBP MFI
J
NTg
250 µm
Tg-ATG13

◂**Fig. 7** Evaluations of inflammatory changes in Tg-ATG13 mice. **A** Dual IF analysis of IBA1 and WDFY3 in the biceps muscle of 5- to 6-week-old female wild-type littermate (NTg) and Tg-ATG13 mice ($n=5$/group). White arrows indicate autophagosomes. **B** Dotted boxplot analysis for quantifying WDFY3-ir autophagosomes in the muscle epithelium. A total of 10 images (two images per mouse; $n=5$/group) were included for counting. An unpaired *t*-test revealed ***$p<0.001$ versus NTg. **C** H&E staining in biceps femoris muscle of 5- to 6-week-old female wild-type littermate and Tg-ATG13 mice ($n=3$). **D** DAB immunostaining of IBA1 in blood vessels surrounding the muscle fibers in wild-type and Tg-ATG13 mice. **E** Dual IF analyses of M1Mϕ marker CD40 (red) and macrophage marker IBA1 (green) in muscle tissue of 5- to 6-week-old female wild-type and Tg-ATG13 ($n=5$) mice. **F** The dotted boxplot represents the quantification of IBA1-ir and CD40-ir cells in per sq. mm. area of muscle epithelium. A total of 10 images (two images per animal; $n=5$/group) were analyzed in both NTg and Tg-ATG13 mice. An unpaired *t*-test was performed to test the significance of the mean between the two groups, which resulted in ****$p<0.0001$ vs. NTg. **G** Representative image was a dual IF analysis of IBA1 and Y705PSTAT3 in biceps muscle tissue of 5- to 6-week-old female NTg and Tg-ATG13 mice ($n=5$). Nuclei were stained with DAPI. **H** A representative image of dual IF staining of myelin marker MBP and axonal marker TUJ1 in nerve bundles of NTg and Tg-ATG13 female mice. **I** A parametric Pearson correlation analysis of MFIs between MBP- and TUJ1-ir nerve fibers. Mean Fluorescence Intensities (MFI) of MBP were measured at ImageJ software in total 40 nerve fibers were randomly included (20 NTg + 20 Tg-ATG13; $n=5$ mice per group)) and then plotted as a scatter plot. **J** LFB staining of spinal cord sections of 5- to 6-week-old wild-type and Tg-ATG13 mice. Results are mean ± SEM of three independent experiments in $n=5$ animals per group

male mice showed mild to moderate weakness. The fatigue was observed to be severe in female mice treated with 5 and 10 mg/kg bwt doses. The dosing regimen was optimized after three stages of experiments. Initially, daily dosing of 10 mg/kg bwt dose of MHY1485 caused significant mortality in 3- to 4-week-old female mice. To reverse mortality, we repeated the same dosing experiment in 5- to 6-week-old mice. The morality was nullified; however, we did not observe any pathology in 5- to 6-week-old female mice. In the final attempt, 3- to 4-week-old mice were dosed with 2, 5, and 10 mg/kg bwt of MHY1485 on every alternate day for 2 weeks. Interestingly, that dosing regimen not only reversed mortality but generated fatigue pathology in mice starting from the 3rd dose. Both 5 and 10 mg/kg bwt MHY1485 generated significant fatigue predominantly in female mice. However, the 10 mg/kg dose was not continued as the 5 mg/kg dose displayed comparable pathology without any mortality. The severe fatigue pathology persisted until 2 weeks after the last dose. The extreme fatigue was evaluated with moderate to severe loss of movement, the reduction of grip strength, and low-frequency EMG waves. We also observed a significant loss of muscle growth evaluated with no gain in body weight and length. We also observed hindlimb clasping in severely fatigued mice, indicating the potential spinal cord pathologies. Muscle fatigue was evaluated with decreased grip strength latency, slowness in movement, and myokymic EMG waves in the biceps femoris muscle. However, this fatigue is transient, and after 2 weeks of the last dose, mice recovered from movement deficit and started to recover body weight.

Chronic activation of mTOR and post-exertional fatigue

Exercise is an integral part of our healthy lifestyle, and studies suggest that routine exercise can prevent cognitive and motor deficits. Reports indicate that mild and long-term treadmill exercise improves cognitive abilities in patients [28, 29] with Alzheimer's disease (AD), ameliorates motor deficit in patients [30] [31] with Parkinson's disease (PD), and helps faster recovery from traumatic brain injury (TBI) [32–34] and stroke [35–37]. Treadmill exercise also benefits patients with osteoarthritis and chronic arterial diseases. Among all these health benefits, treadmill exercises prove to be damaging in many ME/CFS patients with difficulties in maintaining an upright posture, which is clinically termed post-exertional malaise, or PEM. While analyzing post-exertional fatigue in these mice after 1 week of the last dose of MHY1485, these mice were subjected to a single-session treadmill exercise at a speed of 14 rpm for 15 min. Interestingly, 5 mg/kg MHY1485-dosed female mice displayed a complete loss of muscle strength or "crash" pathology immediately after treadmill exercise as evaluated by track-plot analysis. Two days of complete rest followed by similar track plot studies revealed a severe loss of muscle strength in MHY1485-fed mice. In 40% of cases ($n=2$ out of 5 MHY1485-fed female mice), this post-exertional fatigue existed even after 4 days of a single-session treadmill exercise. MHY1485-fed mice displayed severe myokymic changes in muscle tissue as indicated by surface EMG recording in the biceps femoris leg muscle. Myokymic changes in MHY-fed mice displayed low-frequency waves with periodic bursts, which became more prominent after treadmill exercise. Myokymic EMG waves indicated that there was inflammatory demyelination in muscle-serving nerve fibers.

The critical role of autophagy impairment in muscle fatigue

While investigating the molecular mechanism, we first identified that the chronic activation of mTORC1 impaired autophagy via phosphorylation and inactivation of ATG13. *First*, IB analyses revealed that 5 mg/kg dosing of MHY1485 for 2 weeks increased S2448 phosphorylation without changing the protein levels of total mTOR and Raptor, indicating the chronic activation of the mTORC1 complex. *Second*, a subsequent IB analysis revealed that the activated mTORC1 induced the phosphorylation at the S355 residue of ATG13, suggesting the potential inactivation of ATG13 in muscle

tissue. *Third*, an IP followed by IB analysis between HA-ULK1 and FLAG-ATG13 further confirmed that MHY1485 treatment significantly compromised the ATG13-dependent early autophagy complex formation. Moreover, a relative quantitative estimation of LC3 II-*ir* autophagosomes and LysoTracker^{+ve} lysosomes also revealed that MHY1485 treatment significantly attenuated the numbers of de novo synthesized LC3II-*ir* autophagosomes without altering the numbers of lysosomes in HEK293T cells transfected with eGFP-LC3, further suggesting the role of mTOR activation in the inhibition of newly synthesized autophagosomes and subsequent autophagy impairment. Although a previous report (22,927,967) suggested that 2 μM MHY-1485 impaired the fusion of LC3-ir autophagosomes with lysosomes, we observed that 5 μM MHY-1485 inhibited the formation of LC3-II-ir autophagosome without inducing a cytotoxic response in cells. Accordingly, an IB analysis indicated that the oral administration of 5 mg/kg MHY1485 significantly reduced LC3-II level in muscle tissue of mice kept under fasting conditions for 24 h, further suggesting that the oral administration of MHY1485 suppressed the autophagosome formation in muscle tissue of mice. *Fourth*, immunostaining of autophagosomes by WDFY3, followed by the quantification study, further confirmed that oral administration of MHY1485 indeed impaired the formation of autophagosomes in muscle tissue.

Autophagy impairment often leads to chronic inflammation [22, 38] in many metabolic diseases such as aging [39], cancer [40], neuroinflammatory [41], and autoimmune disorders [23]. However, its role was poorly understood in muscle fatigue. Therefore, next, we wanted to study if the chronic mTOR activation followed by autophagy impairment could also stimulate inflammatory reactions in the muscle tissue of MHY1485-fed mice. One of the downstream targets of mTOR is STAT3 [42]. Accordingly, we observed that MHY1485 stimulated Y705 phosphorylation of STAT3, followed by nuclear translocation and binding to the promoters, causing transcriptional upregulations of IL6 and RANTES. Both IL6 [43, 44] and RANTES [45–54

ATG13 transgenic animals could be a critical tool to study PEM-like pathologies.

Previously, we observed that ME/CFS pathogenesis could be associated with elevated levels of phosphorylated and inactivated ATG13 [7]. ATG13 plays a critical role in the mTORC1-mediated inhibition of autophagy. Phosphorylation of ATG13 followed by its functional inactivation and subsequent abortion from the early autophagy complex caused autophagy impairment. Therefore, to explore the potential role of ATG13 inactivation in ME/CFS, we generated a knockout first ATG13 transgenic or Tg-ATG13 mice in which a lacz transcriptional repressor element was inserted upstream of exon 5, causing suppressed expression of ATG13. The complete knocking-down of the atg13 gene causes embryonic mortality. Therefore, our knockout first Tg-ATG13 mouse model showed a severely suppressed atg13 gene but not complete ablation, resulting in significant suppression of lethality. However, in some cases, we saw nearly-complete penetrance of the transgene that causes significant retardation of muscle growth. To avoid that confounding error, we chose 5- to 6-week-old female Tg-ATG13 mice with incomplete penetrance of transgene having similar body weight (14–15 g) compared to wild-type non-Tg mice. Interestingly, we observed that female Tg-ATG13 mice displayed impaired growth up to 3–4 weeks of age and then started gaining muscle fatigue. While analyzing molecular mechanisms, Tg-ATG13 mice were found to have increased infiltration of M1Mφ in the muscle vasculature followed by a severe demyelinating response in muscle-serving nerve fibers. Evaluation of muscle fatigue in an open-field locomotion study combined with EMG recording analysis also demonstrated that Tg-ATG13 mice were associated with myokymic changes in muscle waves resulting in muscle weakness and slow movement. Next, we were interested in studying if Tg-ATG13 animals display PEM-like pathologies. Both male and female Tg-ATG13 mice displayed muscle fatigue. However, male Tg-ATG13 mice had delayed symptoms and started showing fatigue after 5 months of age, whereas female Tg-ATG13 mice showed muscle fatigue early at 6–8 weeks of age. Tg-ATG13 female mice showed baseline fatigue before treadmill exercise, which worsened immediately after treadmill exercise. Nearly 40% (3 out of 8) of mice showed complete immobility or "crash" after immediate exercise. Interestingly, 2 days of complete rest was unable to fully recover the post-exertional exhaustion in these Tg-ATG13 mice, whereas NTg mice completely recovered.

Drawbacks and future direction

There are several drawbacks in our current manuscript that provide little or less knowledge in understanding the concept of PEM. The term "chronic fatigue" is broad, heterogeneous, and the endpoint outcome of many metabolic diseases. Our model highlights a specific molecular mechanism that underlines how the inactivation of ATG13 and subsequent autophagy impairment cause demyelination and muscle weakness. There is a huge role of cardiovascular abnormalities in chronic fatigue, which was not explored in this paper. Therefore, it will be far-fetched and premature to conclude that our model satisfies the clinical hallmarks of PEM. *Second*, we observed a diverse range of chronic symptoms in male Tg-ATG13 mice, such as hair loss or baldness, obesity, and infertility, which are not yet established in chronic fatigue syndrome. *Third*, in our model, the post-exertional fatigue is transient and sustains

no longer than a week. However, in patients, the PEM persists for weeks and even longer. Nevertheless, our model highlights a specific component of muscle fatigue, which is the chronic demyelination in muscle-serving nerve fiber, and also highlights how that deficiency causes severe muscle fatigue after treadmill exercise. Being encouraged by our finding in deciphering the critical role of mTOR activation in ME/CFS, recently we have launched a pilot clinical trial of rapamycin (https://clinicaltrials.gov ID# NCT06257420) in ME/CFS patients who have impaired ATG13 metabolism. We screen ME/CFS patients with an autophagy antibody array to detect elevated non-functional ATG13 levels in their serum samples. The blood collection has already been started, and the initial screening process is currently in progress. After initial screening, the patients will be treated with a low dose of rapamycin for 1 month by certified clinicians, followed by serum collection and subsequent detection of ATG13. The metabolic normalization of ATG13 will then be correlated with their behavioral and symptomatic improvements.

Therefore, taken together, our study delineated how chronic activation of mTOR played a critical role in the inhibition of ATG13 activation, impairment of autophagy, induction of STAT3-mediated inflammation, and augmentation of subsequent demyelinating response in muscle tissue causing chronic muscle fatigue.

Supplementary Information The online version contains supplementary material available at https://doi.org/10.1007/s12026-024-09557-7.

Acknowledgements We are grateful to Milwaukee Institute for Drug Discovery (MIDD) for providing support during the study. The authors thank Jennifer L. Nemke (Animal Resource Center at UWM) for her guidance and support. Authors also thank Audrey Ryback from the University of Edinburgh and Inga Williams from the University of Oxford in assisting the pharmacokinetic studies for MHY1485 drug metabolism.

Author contribution A.R. conceived the idea. M.E.D., S.B., C.G.G., and A.R. designed, performed research, and wrote the manuscript. C.G.G. was in charge of gathering human samples and keeping patients' records. D.P. is a clinician, who was responsible for collecting the biospecimen, developing the questionnaires, and receiving IRB approval. L.A. Arnold helped writing manuscript, provided resources and facilitated the collaborative research between UWM and Simmaron at the University of Wisconsin Milwaukee. L.A. Allen helped designing animal study and writing protocol for the presented animal studies. Arnold and Allen are employees of UWM. L.A. Arnold. and L.A. Allen are members of the IACUC committee that approved the IACUC protocols. L.A. Allen is the attending DVM and in charge of the Animal Research Center at UWM. All authors have read and agreed to the published version of the manuscript.

Funding This work was supported by Simmaron Research Inc., a nonprofit 501C research organization, Incline Village, NV 89451, as a result of funds from NIH R21 grant (R21NS129021-01A1) to AR, Ramsay Award 2023 to AR by Solve ME initiative and donation from Foundation Hesse Sibylla, Quebec, QC, Canada.

Data availability There is no electronic datasheet associated with this paper. Raw immunoblots are presented in the supplementary file.

Declarations

Ethics approval This is not a clinical trial but an institutional observational study. The collection of biospecimen, questionnaire guidelines, record keeping, and generation of unique identification numbers was performed by the Western IRB, protocol #20201812. All methods were carried out in accordance with relevant guidelines and regulations. All experimental protocols were approved by a named institutional and/or licensing committee.

Consent to participate Every human subject in this study has provided consent to participate in this study.

Consent for publication All authors provided their consent to publish this original research article.

Conflict of interest A.R., M.E.D., S.B., C.G.G., and D.P. are employees of Simmaron Research INC, a 501C non-profit research organization. L.A. Allen and L.A. Arnold are employees of UWM. The authors declare no competing interests.

References

1. Deumer U-S, Varesi A, Floris V, Savioli G, Mantovani E, López-Carrasco P, et al. Myalgic encephalomyelitis/chronic fatigue syndrome (ME/CFS): an overview. J Clin Med. 2021;10:4786.
2. Holtzman CS, Bhatia S, Cotler J, Jason LA. Assessment of post-exertional malaise (PEM) in patients with myalgic encephalomyelitis (ME) and chronic fatigue syndrome (CFS): a patient-driven survey. Diagnostics. 2019;9:26.
3. Bateman L, Bested AC, Bonilla HF, Chheda BV, Chu L, Curtin JM, et al. Myalgic encephalomyelitis/chronic fatigue syndrome: essentials of diagnosis and management. Mayo Clin Proc. 2021;96:2861–78.
4. Carruthers BM, Jain AK, De Meirleir KL, Peterson DL, Klimas NG, Lerner AM, et al. Myalgic encephalomyelitis/chronic fatigue syndrome: clinical working case definition, diagnostic and treatment protocols. J Chronic Fatigue Syndr. 2003;11:7–115.
5. Bested AC, Marshall LM. Review of myalgic encephalomyelitis/chronic fatigue syndrome: an evidence-based approach to diagnosis and management by clinicians. Rev Environ Health. 2015;30:223–49.

6. Joyce J, Hotopf M, Wessely S. The prognosis of chronic fatigue and chronic fatigue syndrome: a systematic review. QJM. 1997;90:223–33.
7. Gottschalk G, Peterson D, Knox K, Maynard M, Whelan RJ, Roy A. Elevated ATG13 in serum of patients with ME/CFS stimulates oxidative stress response in microglial cells via activation of receptor for advanced glycation end products (RAGE). Mol Cell Neurosci. 2022;120:103731.
8. Mizushima N. The role of the Atg1/ULK1 complex in autophagy regulation. Curr Opin Cell Biol. 2010;22:132–9.
9. Hosokawa N, Hara T, Kaizuka T, Kishi C, Takamura A, Miura Y, et al. Nutrient-dependent mTORC1 association with the ULK1–Atg13–FIP200 complex required for autophagy. Mol Biol Cell. 2009;20:1981–91.
10. Saxton RA, Sabatini DM. mTOR signaling in growth, metabolism, and disease. Cell. 2017;168:960–76.
11. Deleyto-Seldas N, Efeyan A. The mTOR–autophagy axis and the control of metabolism. Front Cell Dev Biol. 2021;9. https://doi.org/10.3389/fcell.2021.655731.
12. Choi YJ, Park YJ, Park JY, Jeong HO, Kim DH, Ha YM, et al. Inhibitory effect of mTOR activator MHY1485 on autophagy: suppression of lysosomal fusion. 2012. https://doi.org/10.1371/journal.pone.0043418.
13. Zhao S, Chen C, Wang S, Ji F, Xie Y. MHY1485 activates mTOR and protects osteoblasts from dexamethasone. Biochem Biophys Res Commun. 2016;481:212–8.
14. Hao E-y, Wang D-h, Chang L-y, Huang C-x, Chen H, Yue Q-x, et al. Melatonin regulates chicken granulosa cell proliferation and apoptosis by activating the mTOR signaling pathway via its receptors. Poult Sci. 2020;99:6147–62.
15. Gottschalk CG, Whelan R, Peterson D, Roy A. Detection of elevated level of tetrahydrobiopterin in serum samples of ME/CFS patients with orthostatic intolerance: a pilot study. Int J Mol Sci. 2023;24:8713.
16. Roy A, Jana M, Corbett GT, Ramaswamy S, Kordower JH, Gonzalez FJ, et al. Regulation of cyclic AMP response element binding and hippocampal plasticity-related genes by peroxisome proliferator-activated receptor α. Cell Rep. 2013;4:724–37.
17. Ghosh A, Roy A, Liu X, Kordower JH, Mufson EJ, Hartley DM, et al. Selective inhibition of NF-κB activation prevents dopaminergic neuronal loss in a mouse model of Parkinson's disease. Proc Natl Acad Sci. 2007;104:18754–9.
18. Bolintineanu SL, Puscasiu DA, Petrescu CI, Tatu RF, Pop E, Tatu CS, et al. Injected and colouring substances largely used in processing microscopic anatomical structures. Materiale Plastice. 2017;54:505.
19. Roy A, Jana M, Kundu M, Corbett GT, Rangaswamy SB, Mishra RK, et al. HMG-CoA Reductase inhibitors bind to PPARalpha to upregulate neurotrophin expression in the brain and improve memory in mice. Cell Metab. 2015;22:253–65.
20. Jung CH, Jun CB, Ro SH, Kim YM, Otto NM, Cao J, et al. ULK-Atg13-FIP200 complexes mediate mTOR signaling to the autophagy machinery. Mol Biol Cell. 2009;20:1992–2003.
21. Qian M, Fang X, Wang X. Autophagy and inflammation. Clin Transl Med. 2017;6:1–11.
22. White E, Karp C, Strohecker AM, Guo Y, Mathew R. Role of autophagy in suppression of inflammation and cancer. Curr Opin Cell Biol. 2010;22:212–7.
23. Jones SA, Mills KH, Harris J. Autophagy and inflammatory diseases. Immunol Cell Biol. 2013;91:250–8.
24. Yang Z, Goronzy JJ, Weyand CM. Autophagy in autoimmune disease. J Mol Med. 2015;93:707–17.
25. Zhou X-J, Zhang H. Autophagy in immunity: implications in etiology of autoimmune/autoinflammatory diseases. Autophagy. 2012;8:1286–99.
26. Ouédraogo ZG, Müller-Barthélémy M, Kemeny JL, Dedieu V, Biau J, Khalil T, et al. STAT3 Serine 727 phosphorylation: a relevant target to radiosensitize human glioblastoma. Brain Pathol (Zurich, Switzerland). 2016;26:18–30.
27. Kim JH, Kim JE, Liu HY, Cao W, Chen J. Regulation of interleukin-6-induced hepatic insulin resistance by mammalian target of rapamycin through the STAT3-SOCS3 pathway. J Biol Chem. 2008;283:708–15.
28. Arcoverde C, Deslandes A, Moraes H, Almeida C, Araujo NB, Vasques PE, et al. Treadmill training as an augmentation treatment for Alzheimer's disease: a pilot randomized controlled study. Arq Neuropsiquiatr. 2014;72:190–6.
29. Anderson HS, Kluding PM, Gajewski BJ, Donnelly JE, Burns JM. Reliability of peak treadmill exercise tests in mild Alzheimer disease. Int J Neurosci. 2011;121:450–6.
30. Mehrholz J, Kugler J, Storch A, Pohl M, Elsner B, Hirsch K. Treadmill training for patients with Parkinson's disease. Cochrane Database Syst Rev. 2015:CD007830. https://doi.org/10.1002/14651858.CD007830.pub3.
31. Bhalsing KS, Abbas MM, Tan LCS. Role of physical activity in Parkinson's disease. Ann Indian Acad Neurol. 2018;21:242–9.
32. Kim DH, Ko IG, Kim BK, Kim TW, Kim SE, Shin MS, et al. Treadmill exercise inhibits traumatic brain injury-induced hippocampal apoptosis. Physiol Behav. 2010;101:660–5.
33. Silva LF, Hoffmann MS, Gerbatin Rda R, Fiorin Fda S, Dobrachinski F, Mota BC, et al. Treadmill exercise protects against pentylenetetrazol-induced seizures and oxidative stress after traumatic brain injury. J Neurotrauma. 2013;30:1278–87.
34. Seo TB, Kim BK, Ko IG, Kim DH, Shin MS, Kim CJ, et al. Effect of treadmill exercise on Purkinje cell loss and astrocytic reaction in the cerebellum after traumatic brain injury. Neurosci Lett. 2010;481:178–82.
35. Vanderbeken I, Kerckhofs E. A systematic review of the effect of physical exercise on cognition in stroke and traumatic brain injury patients. NeuroRehabilitation. 2017;40:33–48.
36. Duncan PW, Sullivan KJ, Behrman AL, Azen SP, Wu SS, Nadeau SE, et al. Body-weight-supported treadmill rehabilitation after stroke. N Engl J Med. 2011;364:2026–36.
37. Pang MY, Charlesworth SA, Lau RW, Chung RC. Using aerobic exercise to improve health outcomes and quality of life in stroke: evidence-based exercise prescription recommendations. Cerebrovasc Dis. 2013;35:7–22.
38. Lin T-A, Wu VC-C, Wang C-Y. Autophagy in chronic kidney diseases. Cells. 2019;8:61.
39. Salminen A, Kaarniranta K, Kauppinen A. Inflammaging: disturbed interplay between autophagy and inflammasomes. Aging (Albany NY). 2012;4:166.
40. Chen H-Y, White E. Role of autophagy in cancer prevention. Cancer Prev Res. 2011;4:973–83.
41. Alirezaei M, Kemball CC, Whitton JL. Autophagy, inflammation and neurodegenerative disease. Eur J Neurosci. 2011;33:197–204.
42. Vella A, D'Aversa E, Api M, Breveglieri G, Allegri M, Giacomazzi A, et al. mTOR and STAT3 pathway hyper-activation is associated with elevated interleukin-6 levels in patients with Shwachman-Diamond syndrome: further evidence of lymphoid lineage impairment. Cancers 2020;12. https://doi.org/10.3390/cancers12030597.
43. Ishihara K, Hirano T. IL-6 in autoimmune disease and chronic inflammatory proliferative disease. Cytokine Growth Factor Rev. 2002;13:357–68.
44. Gabay C. Interleukin-6 and chronic inflammation. Arthritis Res Ther. 2006;8:1–6.
45. Conti P, DiGioacchino M. MCP-1 and RANTES are mediators of acute and chronic inflammation. Allergy Asthma Proc. 2001;22. https://doi.org/10.2500/108854101778148737. OceanSide Publications.

46. Dutta D, Kundu M, Mondal S, Roy A, Ruehl S, Hall DA, et al. RANTES-induced invasion of Th17 cells into substantia nigra potentiates dopaminergic cell loss in MPTP mouse model of Parkinson's disease. Neurobiol Dis. 2019;132:104575.
47. Roy A, Mondal S, Kordower JH, Pahan K. Attenuation of microglial RANTES by NEMO-binding domain peptide inhibits the infiltration of CD8+ T cells in the nigra of hemiparkinsonian monkey. Neuroscience. 2015;302:36–46.
48. Kistner TM, Pedersen BK, Lieberman DE. Interleukin 6 as an energy allocator in muscle tissue. Nat Metab. 2022;4:170–9.
49. Ishiuchi Y, Sato H, Komatsu N, Kawaguchi H, Matsuwaki T, Yamanouchi K, et al. Identification of CCL5/RANTES as a novel contraction-reducible myokine in mouse skeletal muscle. Cytokine. 2018;108:17–23.
50. Nara H, Watanabe R. Anti-inflammatory effect of muscle-derived interleukin-6 and its involvement in lipid metabolism. Int J Mol Sci. 2021;22. https://doi.org/10.3390/ijms22189889.
51. Belizário JE, Fontes-Oliveira CC, Borges JP, Kashiabara JA, Vannier E. Skeletal muscle wasting and renewal: a pivotal role of myokine IL-6. Springerplus. 2016;5:619.
52. Chabas D, Baranzini SE, Mitchell D, Bernard CC, Rittling SR, Denhardt DT, et al. The influence of the proinflammatory cytokine, osteopontin, on autoimmune demyelinating disease. Science. 2001;294:1731–5.
53. Peterson LK, Fujinami RS. Inflammation, demyelination, neurodegeneration and neuroprotection in the pathogenesis of multiple sclerosis. J Neuroimmunol. 2007;184:37–44.
54. Lu J-Q, Ringrose J, Gross D, Emery D, Blevins G, Power C. Multifocal inflammatory demyelination in a patient with rheumatoid arthritis and treatment complications. J Neurol Sci. 2016;367:305–7.